# PENETRATION RESISTANCE OF POLYMER CROSSLINKED AEROGEL ARMOR SUBJECTED TO PROJECTILE IMPACT

By

SARAH ELIZABETH STAGGS

Master of Science in Mechanical Engineering

Oklahoma State University

Stillwater, OK

2009

Submitted to the Faculty of the
Graduate College of the
Oklahoma State University
in partial fulfillment of
the requirements for
the Degree of
MASTER OF SCIENCE
December, 2009

PENETRATION RESISTANCE OF POLYMER CROSSLINKED AEROGEL ARMOR SUBJECTED TO PROJECTILE IMPACT

Thesis Approved:

Hongbing Lu

Thesis Adviser

Kaan Kalkan

Sandip Harimkar

A. Gordon Emslie

Dean of the Graduate College

# ACKNOWLEDGMENTS

I wish to express my gratitude to my family for their confidence in me. I would like to thank them for their continuous encouragement and love. I would like to express my deepest gratitude to my husband, Ahmed Abd Elfattah, and daughter, Alexandria Hamilton, for their inspiration, patience, support, and understanding.

I would like to express my sincere thanks to my advisor, Dr. Hongbing Lu for his supervision, constructive guidance, financial support, wonderful work environment and inspiration throughout this study. My master's study under him has been a great experience. I would also like to extend my sincere appreciation to Dr. Jay Hanan for providing invaluable guidance and encouragement throughout this study.

This project has been funded by grants from the Naval Research Laboratories (N0173-07-1-G001) and the National Science Foundation (CMMI-19468). I would like to thank Jack Frost for his abundant knowledge and willingness to help in this study.

I wish to thank Mr. Gitogo Churu for his cooperation, knowledge, and guidance in this study. I would like to thank my research colleagues: Vijay Subramanian, Boshen Fu, Dr. Huiyang Luo, Dr. Yong Wang, Balaji Jayakumar, Advait Bhat, and many others for their help and encouragement.

I would like to thank Servant Medical Imaging of Stillwater, OK for their time and dedication to this work. Their services have proven to be invaluable to me and the results I have obtained.

I would like to thank Sgt. Steve Hoffman and the Stillwater Police Department for their willingness to test for us throughout the duration of this project. Their time and knowledge are greatly appreciated and have contributed to the success of this study.

I would like to thank the Department of Mechanical and Aerospace Engineering for providing me with the opportunity to pursue a Master of Science at Oklahoma State University.

I wish to thank God for His grace and mercy. Without Him, this work could not be completed.

Finally, I wish to dedicate this work to my brother, David Staggs. Thank you for all of your encouraging words and always challenging me to be better. I will always strive to reach the level of intelligence that came to you so easily. Although you were not able to watch this work come to fruition, I know that you are looking down on me with a big smile on your face.

TABLE OF CONTENTS

LIST OF TABLES

Table Page

LIST OF FIGURES

Figure Page

Figure Page

# 1. INTRODUCTION

Military body armor is constantly under evaluation, research, and design. Creating a lightweight body armor which protects against the most threatening and dangerous types of ammunition is the main goal of every researcher in this field of study. Currently employed body armor is heavy and in some instances fails. The continuous change in tactics calls for military body or vehicle armor to undergo constant evaluation and improvement. While strength and endurance are vital to successful armor, the weight of the body armor is critical. As technology advances, smart armor and lightweight designs will begin to emerge. Aerogel is considered to be one of the lightest materials. But traditional aerogels are brittle, rendering it not suitable for armor applications. Aerogel is a porous material with excellent material properties. Leventis developed a new, polymer crosslinked aerogel (Nanoletters, 2002). To date, more than 30 types of aerogels were crosslinked with polymers (Leventis, 2007). After the crosslinking process was complete, Leventis performed a three-point flexural bending test on the aerogel samples. The test results show that it takes 100 times higher load to break the crosslinked aerogel when compared with native aerogel when the density increases by three times. Although the modulus of elasticity was measured in native aerogel, through the measurement of wave speed, it was found that the wave speed is on the order of 100 m/s (328 ft/s), giving a Young's modulus on the order of 1 MPa (145 psi). Leventis measured the modulus of the crosslinked aerogel through flexural bending test (Leventis 2007).

## Research Objective

The purpose of this study is to incorporate this new type of aerogels, namely crosslinked aerogels, into body armor to evaluate its performance, with the eventual objective of reducing weight of body armor.

## 2. REVIEW OF LITERATURE

Research is continually being conducted to improve current body armor. The objectives of improved body armor are to reduce weight, reduce thickness, and reduce back face deflection. Many different types of materials are being considered to meet these objectives.

Capadona et al. (2006) report a study centered on the improvements in mechanical properties obtained when building polymer crosslinking on a lower density silica framework. In this work, twenty-eight different aerogel monoliths were prepared where three preparation conditions were systematically varied: silane concentration (s) at four different levels, di-isocyanate concentration (d) at four levels and polymerization temperature (t) at two levels (Capadona et al. 2006). Results from this study conclude that the highest density crosslinked aerogel had the highest stress at failure and highest modulus, and the stress at failure was 120 times higher than that of non-crosslinked aerogels while density increased by a factor of three (Capadona et al. 2006). The lowest density crosslinked aerogels exhibited a 15-fold increase in stress at failure with a factor of ~1.3 increase in density (Capadona et al. 2006). Figure 1 gives the stress-strain curves for a higher modulus sample and a lower modulus sample.

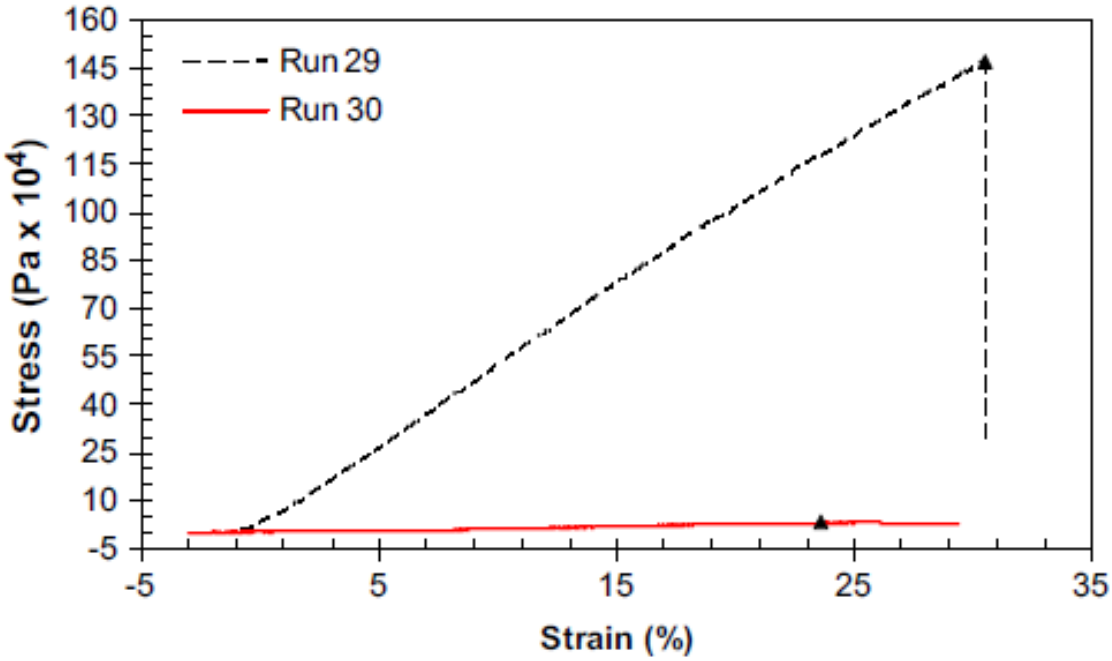


Figure 1: Representative stress-strain curves showing the range in modulus displayed by aerogels with varied amounts of total silane and polymer crosslinking. Black triangles indicate initial break points. (Capadona et al. 2006)

As seen in Figure 1, the lower modulus sample displays a more gradual fracture under increased strain while the stiffer material fractures completely under maximum stress (Capadona et al. 2006). Graphs of the response surface models for density and maximum stress at failure and modulus are shown in Figure 2.

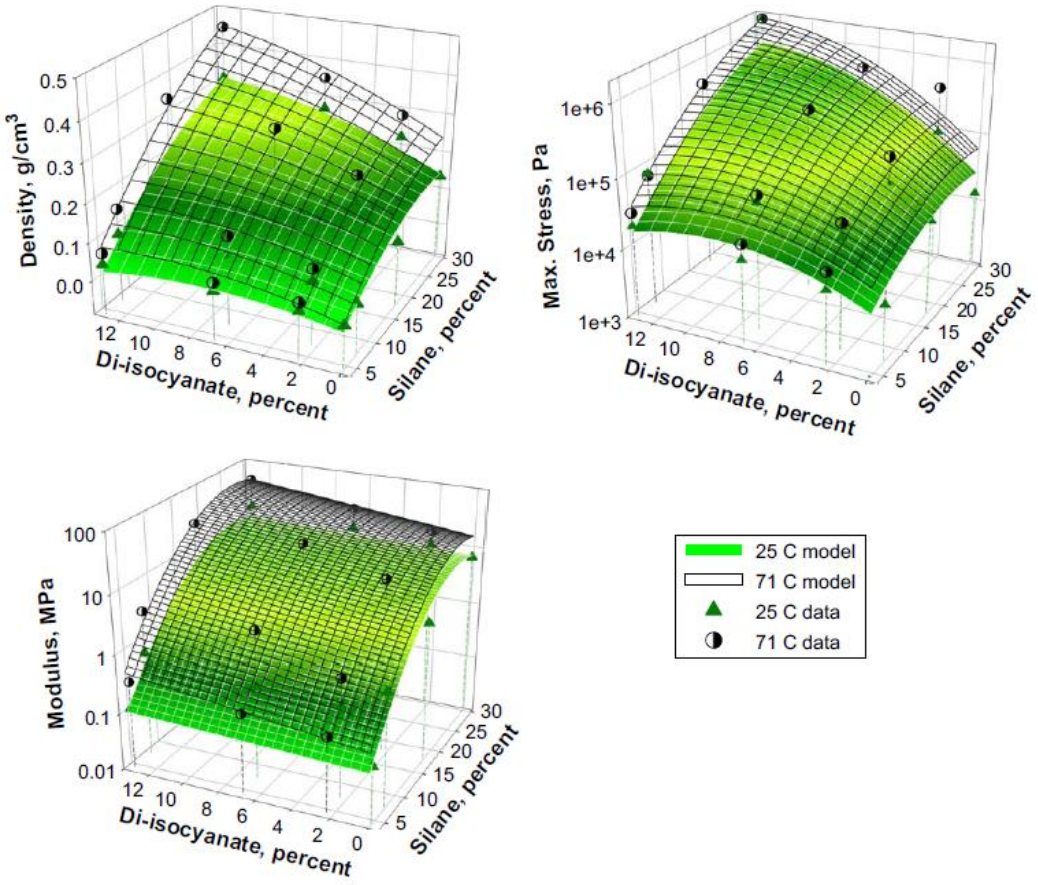


Figure 2: Response surface models density, maximum stress at failure and flexural modulus, plotted vs. the di-isocyanate and the total silane concentration graphed along with experimental data points. (Capadona et al. 2006)

From Figure 2, increasing silane concentration increases all three measured responses. In addition, density and maximum stress at failure show an increase with increasing di-isocyanate concentration (Capadona et al. 2006). For density and maximum stress, the synergistic effect between silane and di-isocyanate concentration (sd) is evident (Capadona et al. 2006). Additionally, Capadona et al. (2006) conclude from Figure 2 that temperature has an effect on all responses. Also, density, maximum stress modulus are higher for all combinations of both di-isocyanate and silane concentrations (Capadona et al. 2006). In this study, Capadona et al. (2006) determined that the highest density native aerogel produced in this study has a calculated porosity of 91.9%. Also, when this

sample was crosslinked using the highest monomer concentration available, the resulting monolith still remains over 75% porous (Capadona et al. 2006). Adversely, the porosity of the lowest density native aerogel is 97.5% with a resulting monolith which is 95.1% porous after crosslinking (Capadona et al. 2006). Capadona et al. (2006) conclude that utilizing empirical models to tailor aerogels with a particular set of properties for a wide variety of applications can be expanded by quantifying a broader range of processing conditions for a host of other properties such as thermal conductivity, compressive strength, density, and stress at failure.

Karamis et al. (2008) investigated the interaction between projectile and metal-matrix composites (MMCs) at a high velocity impact. In their study, two different composites were produced; one by casting and the other by lamination (Karamis et al. 2008). Karamis et al. (2008) manufactured metal matrix composites using Al alloys reinforced with $Al_2O_3$ or SiC. The composites were manufactured by a squeeze casting method where reinforcement particles were incorporated into a liquid matrix material and stirred to achieve a homogeneous mixture in a steel mold (Karamis et al. 2008). The composites were solidified under pressure with resulting dimensions of 120 mm (0.4 ft) in diameter and a thickness of 20 mm (0.07 ft). In addition, laminated composites with SiC particles and a Kevlar back side support were manufactured and tested. The laminated composites had a thickness of 15 mm (0.05 ft) after pressing (Karamis et al. 2008). All targets were tested with an armor piercing projectile with a velocity range of 770 - 800 m/s (2526 – 2625 ft/s). Karamis et al. (2008) concluded that the MMCs can prevent the penetration of a projectile through their body by consuming the projectile's kinetic energy through

damage such as cracking, petalling, and matrix deformation. Also, the reinforcement particles decrease the velocity of the projectile by strong friction generated by scratching the projectile surface. Test results show that the composite could prevent the penetration of the projectile and that even a 20% SiC reinforcement makes the composite strong enough to resist the impact. However, Karamis et al. (2008) did not give back face deflection data for their study.

Katti et al (2006) investigated the chemical, physical, and mechanical characterization of isocyanate crosslinked amine-modified silica aerogels. Their work describes new mechanically strong lightweight porous composite material obtained by encapsulating the skeletal framework of amine-modified silica aerogels with polyurea (Katti et al. 2006). The potential of the new crosslinked silica aerogels for load-carrying applications was determined through characterization of their mechanical behavior under compression, three-point bending and dynamic mechanical analysis (DMA) (Katti et al. 2006). Silica aerogel is a low-density, chemically inert material with low thermal conductivity, excellent acoustic insulation properties (Katti et al. 2006). With these properties, the silica aerogel could be used in different areas such as air/water purification, catalysis, energy storage, sensing, and aerospace applications (Katti et al. 2006). However, due to the fragility of aerogels, they have only limited use such as Cerenkov radiation detectors in certain types of nuclear reactors, in NASA's stardust program for capturing hypervelocity particles in space, and as ultra lightweight thermal insulators aboard planetary vehicles on Mars such as the Sojourner rover in 1997 and the Spirit and Opportunity in 2004 (Katti et al. 2006). Katti et al. (2006) state that future space

exploration will rely on weight reduction and multifunction and that the insulating properties of aerogels in combination with improved mechanical strength could make them an ideal dual-function material. Aerogel fragility is due to their "pearl-necklace" fractal network of secondary silica nanoparticles with densities about half of dense silica (Katti et al. 2006). The large pores in between those chains is responsible for the low density of aerogels and their fragility is due to the interparticle connecting zones or necks (Katti et al. 2006). It is assumed that when the necks are made wider, the specific stiffness and strength of aerogels could be increased without compromising their weight (Katti et al. 2006). In their study, Katti et al (2006) combine amine-functionalized silica with isocyanate chemistry to produce highly porous crosslinked silica aerogels with exceptional mechanical properties characterized through compressive and flexural bending tests. Aerogels for this work were prepared by crosslinking an amine-modified silica framework produced by co-gelation of 3-aminopropyltriethoxysilane (APTES) and tetramethylorthosilicate (TMOS) with the crosslinker being a hexamethylene diisocyanate oligomer (Katti et al. 2006). Katti et al. (2006) used DMA testing at a temperature range between -132 and 200°C to determine glass transition temperatures. They also performed compression tests and flexural bending tests at room temperature as well as lower temperatures with -196°C being the lowest (Katti et al. 2006). After obtaining compression results, Katti et al (2006) converted the load-displacement curves into a stress-strain curve. From this data, they extracted compressive stress at ultimate failure, strain at failure, and Young's modulus (Katti et al. 2006). Data obtained from DMA testing is shown in Figure 3.

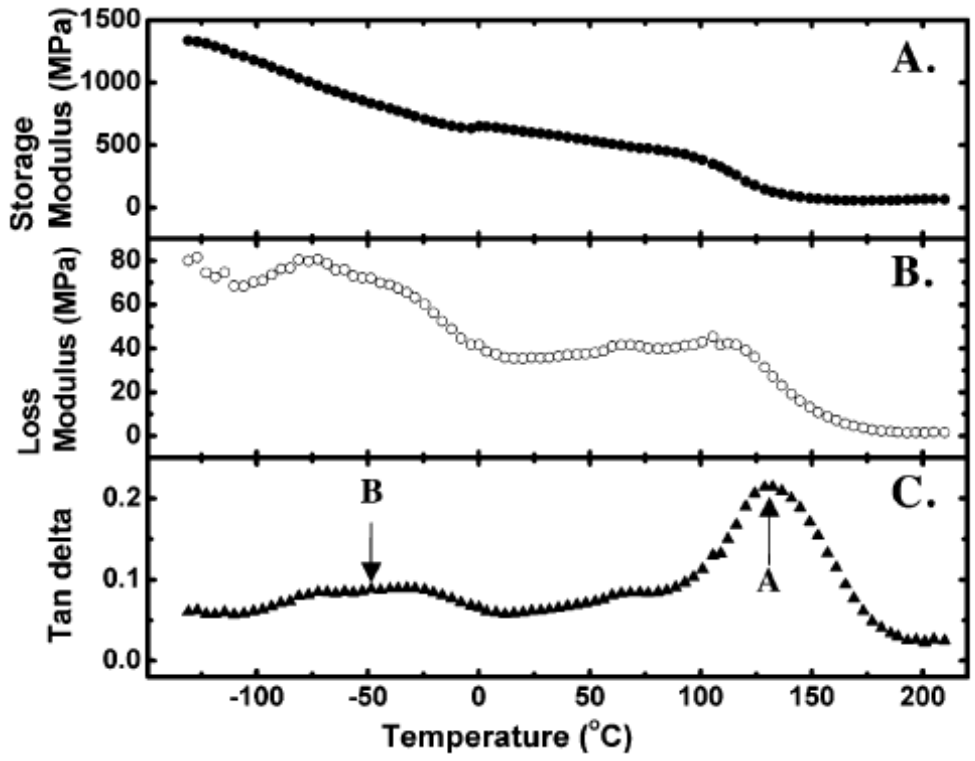


Figure 3: Dynamic mechanical analysis (DMA) on a Desmodur N3200 cross-linked APTES-modified silica aerogel ($\rho \sim 0.67$ g/cm$^3$). Data were collected in a three-point bending mode with loads applied sinusoidaly at 1 Hz. (A) Variation of storage modulus with temperature; (B) Variation of the loss modulus with temperature. (C) Variation of tan (ä) with temperature. (Katti et al. 2006)

Figure 3A shows the storage modulus as a function of temperature where the modulus at room temperature is shown to be 611 MPa. From the graph, the storage modulus decreases with temperature increase and at around -50°C and 130°C it decreases at a steeper rate indicating β and α glass transition temperatures, respectively (Katti et al. 2006). From Figure 3C, there is a peak in tan(δ) at 130°C which indicates the material undergoes softening at that temperature and confirms that this temperature is the major glass transition temperature (Katti et al. 2006). Compression testing was performed on an MTS machine along with high-speed photography. Data on compressive strength, compressive stress at ultimate failure, and Young's modulus are given in Table 1.

Table 1: Summary of Compressive Strength Data of Isocyanate Cross-linked Amine-Modified Silica Aerogels at a Strain Rate of 0.0035/s

| sample number | density ($g \cdot cm^{-3}$) | compressive yield strength (MPa) | compressive stress at final failure (MPa) | failure strain (%) | Young's modulus (MPa) |
|---|---|---|---|---|---|
| 1 | 0.48 | 4.19 | 190.33 | 77.22 | 122.85 |
| 2 | 0.47 | 4.25 | 222.08 | 77.04 | 119.58 |
| 3 | 0.48 | 3.88 | 168.55 | 77.2 | 126.27 |
| 4 | 0.48 | 4.47 | 173.72 | 76.1 | 135.27 |
| 5 | 0.48 | 4.50 | 173.20 | 78.35 | 138.94 |
| average | $0.478 \pm 0.004$ | $4.26 \pm 0.25$ | $186 \pm 22$ | $77.2 \pm 0.8$ | $129 \pm 8$ |

Katti et al. (2006) concluded that the specific compressive yield strength is calculated at 8900 Nm/kg, the specific compressive stress at ultimate failure is 186 MPa yielding a value of $3.89 \times 10^5$ Nm/kg, the Young's modulus of the crosslinked aerogel is $129 \pm 8$ versus $92 \pm 7$ MPa of the native silica framework, a specific Young's modulus of $2.7 \times 10^5$ Nm/kg. Katti et al. (2006) conclude that increased strain rate does not have a deleterious effect on the energy-absorption behavior of aerogels under compression within the range of strain rates tested. This result along with the resilience of the material would suggest aerogels to be used in ballistic applications in addition to more testing at very high strain rates via the split Hopkinson pressure bar (Katti et al. 2006). With regards to flexural testing, Figure 4 shows the stress-strain curves obtained through a three-point bending test.

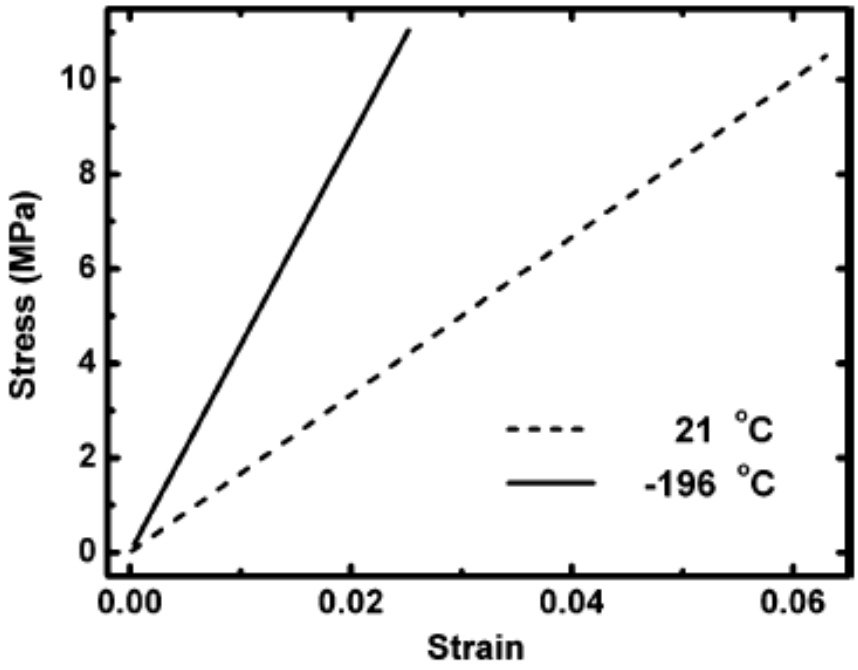


Figure 4: Three-point bending tests on Desmodur N3200 cross-linked APTES-modified silica aerogel rectangular samples with nominal dimensions of 11 × 11 × 50 mm ($\rho \sim 0.48$ g/cm$^3$).

Katti et al. (2006) determined that the average flexural modulus was determined to be 167 MPa at room temperature, the flexural modulus was almost doubled at cryogenic temperatures, and that they flexural strength (~11 MPa) increases slightly at cryogenic temperatures. Katti et al. (2006) also conclude that the test results of their study indicate that these materials be used for the dual purpose of a thermal insulator/structural component with applications wherever weight reduction is critical.

Kaufmann et al. (2003) presented test results where penetration tests were conducted on four different ceramic materials including: alumina, modified alumina, silicon carbide, and boron carbide. The ceramic tiles were bonded to aluminum cylinders and impacted with armor piercing projectiles. Table 2 gives the thickness and areal density of the tested ceramic tiles.

Table 2: Thickness and areal density of ceramic tiles tested by Kaufmann et al. (2003)

| Ceramic type | Thin example | | Thick example | |
|---|---|---|---|---|
| (–) | (mm) | ($kg/m^2$) | (mm) | ($kg/m^2$) |
| CERAMOR | 8.73 | 31.97 | 14.77 | 54.26 |
| CERAMOR Z | 8.63 | 32.33 | 14.83 | 55.6 |
| HEXOLOY | 11.42 | 36.03 | 17.75 | 56.13 |
| Ceralloy 546 | 15.25 | 38.32 | 22.87 | 57.41 |

The silicon carbide tile tested was Hexoloy. For the above data, the areal density for the Hexoloy in English units is 7.3 $lb/ft^2$ for the thin example and 11.45 $lb/ft^2$ for the thick example. In their study, Kaufmann et al. (2003) used Depth of Penetration (DOP) testing to evaluate the ballistic performance of the four ceramics. A DOP value was obtained by measuring the depth of the impact crater in the backing material of protected and unprotected targets (Kaufmann et al. (2003). The backing used in these tests was 6061-T6 aluminum cylinders with dimensions of 152 mm (0.5 ft) long and a diameter of 152 mm (0.5 ft) (Kaufmann et al. 2003). The DOP experiments were conducted at three different velocities. For DOP results at an impact velocity of 750 m/s (2460.6 ft/s), the tiles protected by silicon carbide had the smallest depth of penetration. For impact velocities of 850 m/s (2788.7 ft/s) and 910 m/s (2985.6 ft/s), the silicon carbide and boron carbide had similar DOPs which were approximately five times better than the alumina materials. Kaufmann et al. (2003) have also observed that the efficiency of the silicon carbide and boron carbide increase as impact velocity increase. In addition, it is noted that silicon carbide outperforms all other ceramics at all impact velocities.

Aerogels are considered low-density, highly nano-porous materials with high strength. Since thermal, physical, and mechanical properties of aerogels have already been established, Luo et al. (2006) present the results on the dynamic compressive behavior of crosslinked silica aerogel (CSA) using a split Hopkinson pressure bar (SHPB). Luo et al. (2006) state that the polymer crosslinked aerogel can be up to three times more dense, but more than 300 times stronger and less than one tenth as hydrophilic as native aerogels. Their study determined the stress-strain relation of dry CSA at several high strain rates. From the testing, Luo et al. (2006) used high speed photography and Digital image correlation (DIC) to observe the deformation and failure behavior as well as analyze the deformation and strain fields. All dynamic compressive tests were conducted in ambient conditions. The stress-strain curves for CSA of 0.452 g/cm$^3$ at several strain rates within 114-4386/s are shown in Figure 5 (Luo et al. 2006).

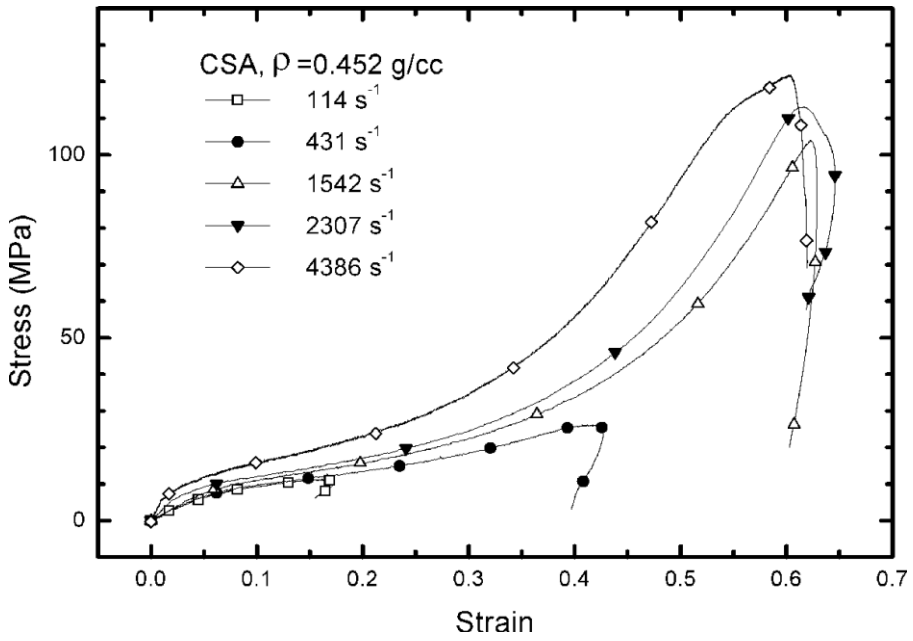


Figure 5: Compressive stress-strain curves at different strain rates (Luo et al. 2006)

Results indicate that the mechanical behavior of CSA depends on the strain rate and the stress-strain curves at higher strain rates are generally higher than that at lower rates, indicating a stiffening behavior as strain rate increases within these rates (Luo et al. 2006). Luo et al. (2006) observed that the CSA samples are linearly elastic at small compressive strains, yield and then exhibit plastic hardening and fail at 60 – 65% compressive strain. This yields an ultimate compressive strength of 405 ± 5 MPa, 113 ± 6 MPa, and 120 ± 7MPa at strain rates of 1542, 2307, and 4386/s (Luo et al. 2006). Young's modulus data and the 0.2% offset compressive yield strengths are shown in Table 3 and plotted in Figure 6 as a function of strain rate (Luo et al. 2006).

Table 3: CSA Young's modulus and 0.2% offset compressive yield strengths at several strain rates (Luo et al. 2006)

| Strain rate ($s^{-1}$) | 114 | 431 | 1542 | 2307 | 4386 |
|---|---|---|---|---|---|
| Young's modulus (MPa) | 133.2 ± 13.3 | 191.7 ± 24.2 | 217.4 ± 26.3 | 289.7 ± 39.0 | 498.1 ± 56.8 |
| Yield strength (MPa) | 6.0 ± 0.12 | 6.32 ± 0.14 | 6.55 ± 0.15 | 6.89 ± 0.15 | 7.05 ± 0.18 |

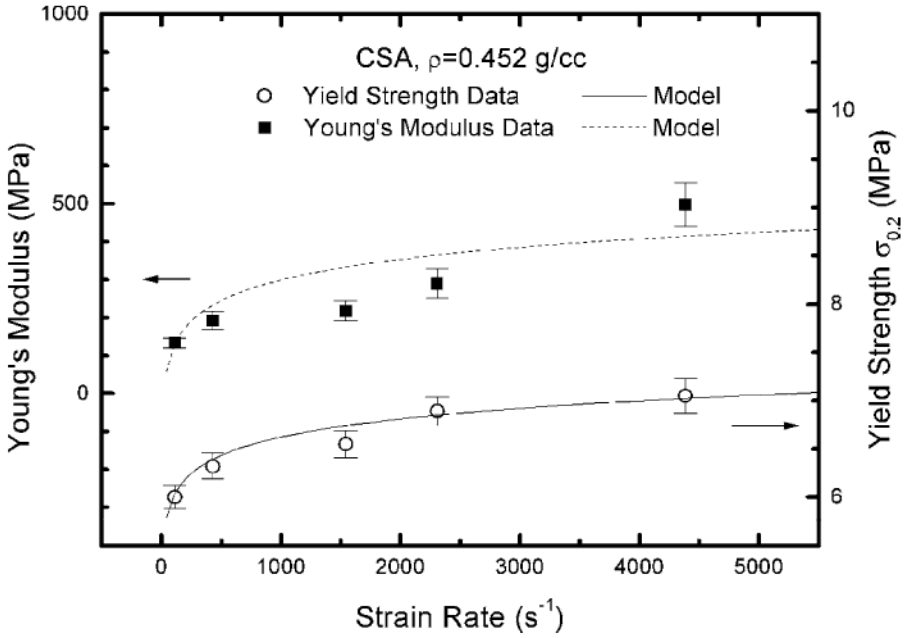


Figure 6: Young's modulus and yield strength as a function of strain rate. Note that the Young's modulus at strain rate of 4386 s−1 is not reliable as dynamic equilibrium was not established within limit of linearity (Luo et al. 2006)

From Figure 6 it can be seen that yield strength and Young's modulus increase with the strain rate. Luo et al. (2006) also explored the effects of mass-density on the stress-strain relationship. Figure 7 shows the stress-strain curve of native silica aerogel with density 0.472 g/cm$^3$ (Luo et al. 2006).

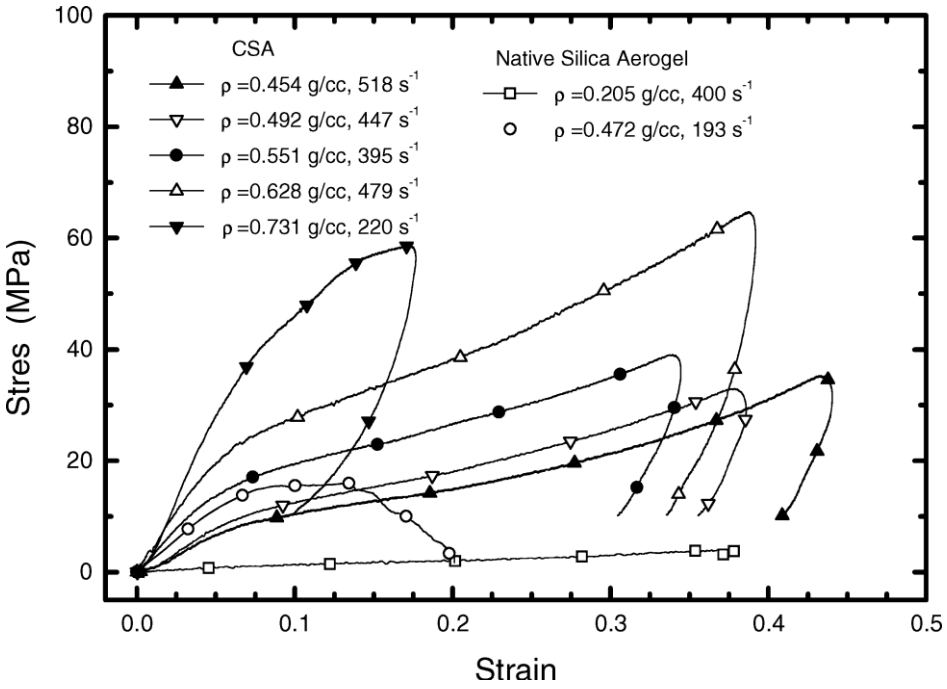


Figure 7: Effects of mass density on compressive stress-strain relation of CSA at several strain rates (average is close 350/s) (Luo et al. 2006)

The native silica aerogel has higher Young's modulus (226.8 ± 16.4MPa) and yield strength (9.63 ± 0.98MPa) than the corresponding values of a typical CSA of approximately the same density, but the native aerogel has low ultimate compressive strength (14.35 ± 2.35MPa) and failure compressive strain (17.8 ± 0.8%) (Luo et al. 2006). Luo et al. (2006) also examined the effects of specimen thickness on the stress-strain relation and dynamic stress equilibrium condition. During experimentation, Luo et al. (2006) used different thicknesses to determine whether the stress-strain relation was affected by the sample thickness. Cylindrical samples with diameter 12.67mm were used; their thicknesses were 2.54, 5.21, 6.45 and 7.92 mm. Their densities were 0.470, 0.456, 0.468 and 0.459 g/cm3, respectively. Figure 8 shows the stress-strain curves obtained from these samples.

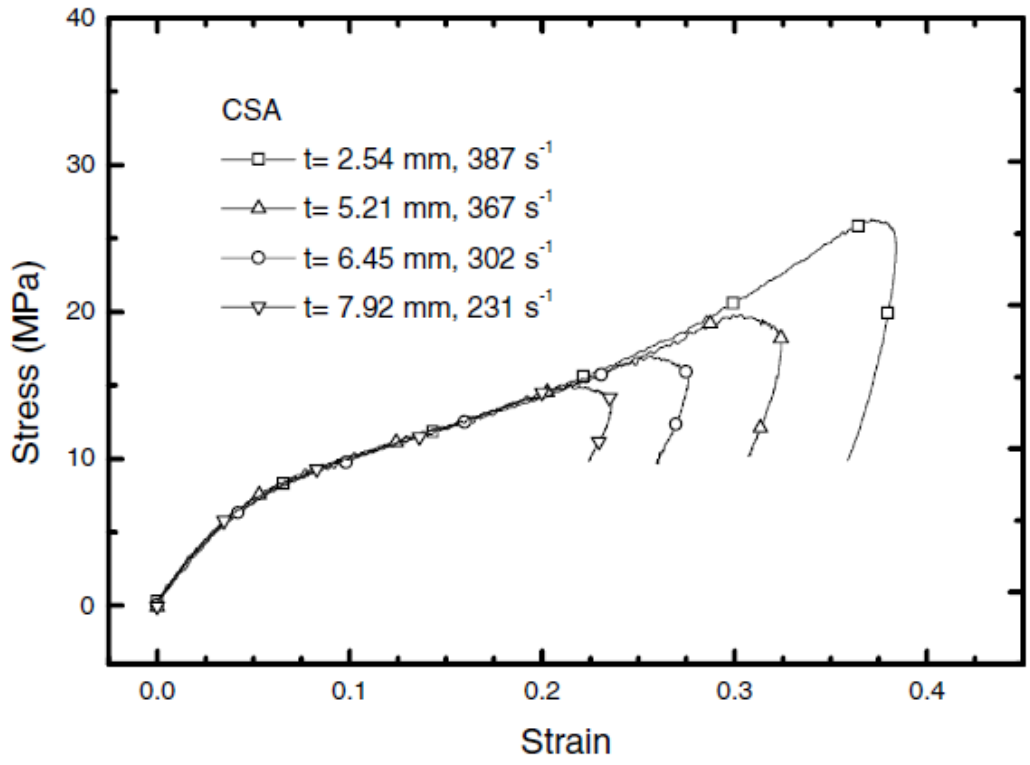


Figure 8: Compressive stress-strain curves obtained with specimens of different thicknesses.

Luo et al. (2006) concluded that the results are independent of sample thickness. In order to validate this conclusion, Luo et al. (2006) checked whether the dynamic stress equilibrium condition is maintained. Luo et al. (2006) concluded that within strain rates 230 – 405/s, the dynamic stress strain curves should not vary, so that the stress-strain relation, obtained for samples with thicknesses between 2.54 and 7.92 mm, is independent of sample thickness. Luo et al. (2006) studied the effects of water absorption on the stress-strain relationship. CSA samples were immersed into water after which they absorbed moisture and reached a saturated state after ~48 hours (Luo et al. 2006). After reaching a fully saturated state, the density of the CSA was 1.110 g/cm$^3$, representing a weight gain of 152% while the volume increased by only 5% (Luo et al. 2006). The saturated samples were tested on the SHPB where, at small strain rates up to

~4.5%, a higher Young's modulus than dry samples (Luo et al. 2006). In addition, the wet samples have lower yield strength than dry samples at a strain of ~5% (Luo et al. 2006). Luo et al. (2006) concluded that the wet sample in general had the stress-strain relation close to a dry sample and at the initial stage with small compressive strains (up to ~4.5%), the wet sample was stiffer. In addition, between ~5% and ~25% compressive strains, the wet CSA was slightly weaker than the dry CSA and at a compressive strain higher than ~25% the wet CSA was slightly stronger than the dry CSA (Luo et al. 2006).

Meador et al. (2005) explore the effects of crosslinking amine-modified silica aerogels with epoxies. In their study, Meador et al. (2005) describe a system where amine functionality is introduced into silica aerogels and the resulting gels are treated with di-, tri-, or tetra-functional epoxies in various concentrations. The reaction conditions are varied along with APTES concentration and epoxy type and concentration (Meador et al. 2005). The resulting gels are dried with supercritical carbon dioxide into aerogels, which are characterized macroscopically, microscopically, and chemically (Meador et al. 2005). Three different percent volume concentrations for each epoxide were used for crosslinking (Meador et al. 2005). The density of the samples was determined from their physical dimensions and their weight (Meador et al. 2005). Surface area and pore diameters were determined by nitrogen absorption porosimetry (Meador et al. 2005). Mechanical strength was obtained by three-point bending and the results as well as density are plotted in Figure 9 and distinguished by epoxy type.

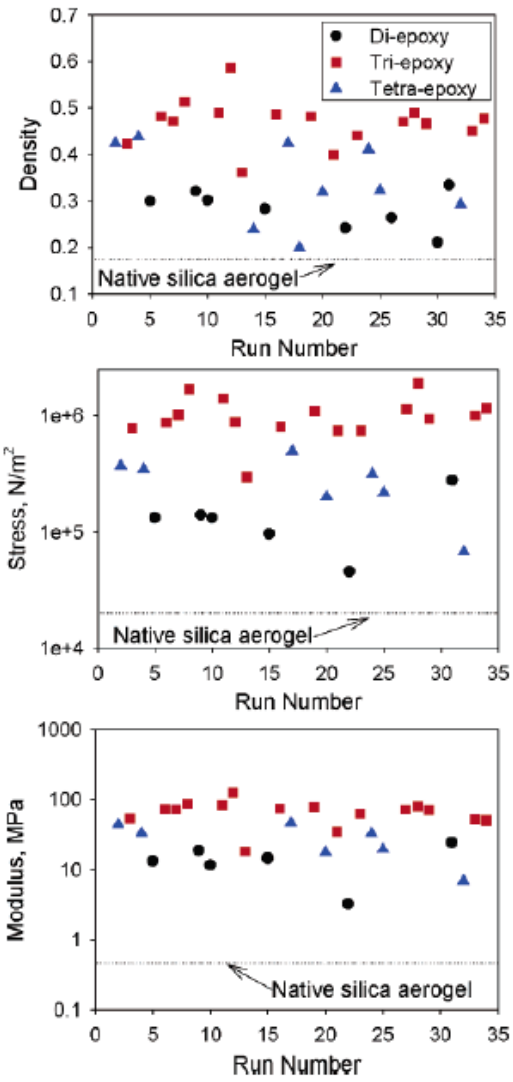


Figure 9: Time series plots of runs from the experimental design compared to native silica aerogels (Meador et al. 2005)

Meador et al. (2005) conclude that these plots dramatically show that while the density of epoxy-crosslinked aerogels is at most 2 - 3 times higher than the density of native silica aerogels, both stress at breakpoint and modulus increase by as much as 2 orders of magnitude. In their study, Meador et al. (2005) find that epoxy crosslinked aerogels appear more elastic and retain higher porosity than their isocyanate counterparts and that the trifunctional epoxide yielded the strongest crosslinked aerogels.

Medvedovski (2006) summarized the achievements in the development of ceramics for personnel armor. The types of ceramics include: alumina, alumina-mullite, silicon carbide, and reaction-bonded silicon carbide. These types of ceramics were chosen due to the following reasons: high physical properties, low cost, density, and ease of production. The microstructural features affect the physical properties and ballistic performance of the ceramics. Ceramic-matrix composites are also considered due to their mechanical properties and their ability to dissipate impact energy. The structure of alumina armor ceramics is uniform and microcrystalline. Phase composition and microstructure consist of corundum grains bonded by a small amount of mullite crystals. The grain size of the ceramic depends on the initial batch composition, initial particle size, and particle size distribution of the powders. Alumina ceramics with high corundum contents and a fine microstructure demonstrate higher values of mechanical properties such as hardness, strength, and Young's modulus. Table 4 gives some physical properties of the studied Alumina ceramics.

Table 4: Physical properties of the studied Alumina and Alumina-Zirconia armor ceramics (Medvedovski 2006)

| Property | AL97ML | AL98 | AL98.5 | AL99.7 | AZ |
|---|---|---|---|---|---|
| Density,* g/cm$^3$ | 3.74- 3.76 | 3.78-3.82 | 3.81-3.84 | 3.90-3.91 | 4.35-4.39 |
| Young's Modulus, GPa | 280-300 | 325-360 | 370-420 | 400-450 | 310-340 |
| Sonic Velocity, km/s | 9.5-9.9 | 10.0-10.5 | 10.6-11.3 | 10.7-11.6 | 9.8-10.0 |
| Vickers Hardness HV10 | 1230-1260 | 1220-1330 | 1320-1420 | 1520-1560 | 1520-1580 |
| Fracture Toughness $K_{Ic}$, MPa.m$^{1/2}$ | 3.0-3.3 | 3.2-3.3 | 3.3-3.4 | 3.1-3.4 | 3.9-4.0 |
| Flexural Strength, MPa | - | 250-350 | 270-360 | 320-380 | 500-560 |
| Brittleness, $B$x10$^{-6}$, m$^{-1}$ | 340-380 | 370-430 | 420-460 | 525-545 | 280-330 |
| Ballistic Energy Dissipation Criterion $D$x10$^{-12}$, 1/s (calculated) | 1.70-1.95 | 1.50-1.60 | 1.80-1.95 | 2.20-2.40 | 1.15-1.20 |

* Water absorption is not greater than 0.02%

For the naming scheme of the Alumina ceramics, the number denotes approximate $Al_2O_3$ content. Alumina-Mullite ceramics have physical properties which are not as high as

alumina ceramics. However, they may be considered promising due to the relatively high properties relevant to ballistic performance, such as lower brittleness and lowest density. Table 5 gives the properties of the studied Alumina-Mullite ceramics.

Table 5: Properties of selected Alumina-Mullite ceramics (Medvedovski 2006)

| Property | AM2 | AM5 | ZAS2 | ZAS3 |
|---|---|---|---|---|
| Density, g/cm$^3$ | 3.52-3.56 | 3.52-3.55 | 3.70-3.75 | 3.58-3.62 |
| Vickers Hardness HV10, kg/mm$^2$<br>GPa | 1130<br>11.1 | 1030<br>10.1 | 1180<br>11.6 | 940<br>9.2 |
| Rockwell Hardness HRA | 90.5 | 89 | 90 | 85 |
| Fracture Toughness $K_{Ic}$, MPa.m$^{1/2}$ | 2.54 | 2.32 | 3.03 | 3.08 |
| Sonic Velocity, km/s | 8.62 | 8.76 | 9.04 | 8.38 |
| Young's Modulus, GPa | 237 | 241 | 275 | 228 |
| Flexural Strength, MPa | 350 | 300 | 350 | 275 |
| Brittleness, $B$x10$^{-6}$, m$^{-1}$ | 408 | 452 | 347 | 221 |
| Ballistic Energy Dissipation Criterion $D$x10$^{-12}$, 1/s | 1.3 | 1.4 | 1.1 | 0.7 |

The values of properties presented are average

The ZAS materials shown in the table are Alumina-Mullite ceramics with additional zircon and zirconia phases (Medvedovski 2006). Silicon carbide based ceramics are developed and selected to achieve an optimal particle size distribution and compaction. These selected materials are distinguished by specific SiC and $Al_2O_3$ contents, by the presence and content of $Si_3N_4$, by the SiC particle size distribution, by the use of sintering aids and by the firing conditions (Medvedovski 2006). These ceramics have higher mechanical properties, due to a higher level of grain compaction and bonding and are more prospective for ballistic applications. They also possess small porosity and relatively high Young's modulus. Table 6 gives the physical properties of SiC-based heterogeneous ceramics.

Table 6: Some physical properties of SiC-based heterogeneous ceramics (Medvedovski 2006)

| Property | Ceramics in the group $SiC-(Si_3N_4)-Al_2O_3$ | Ceramics in the group $SiC-Si_3N_4-Al_2O_3-Si$ |
|---|---|---|
| Density, $g/cm^3$ | 2.7 – 3.2 | 2.85 – 3.05 |
| Rockwell Hardness HRC<br>HRA | 40 – 55<br>58 - 77 | 45 – 55<br>68 – 78 |
| Flexural Strength, MPa | 105 - 155 | 120 – 140 |
| Impact Strength, $kJ/m^2$ | 1.86 – 2.24 | - |
| Young's Modulus, GPa | 240 - 310 | 260 – 280 |
| Sonic Velocity, km/s | 9.8 – 11.2 | 9.8 – 10.05 |

Reaction bonded silicon carbide (RBSC) ceramics are dense and have heterogeneous structure formed by SiC grains of different sizes. Physical properties of RBSC ceramics depend on their structure and phase composition. Their hardness and elastic modulus are relatively high. Their mechanical strength is significantly lower than of SiC materials. The bonding phase composition may play a role in fracturing and ballistic performance. If the bonding matrix in RBSC ceramics has lower hardness, these ceramics have elevated fracturing and elongated cracks upon ballistic impacts resulting in lower ballistic performance (Medvedovski 2006). Table 7 gives physical properties of RBSC ceramics.

Table 7: Some physical properties of RBSC ceramics (Medvedovski 2006)

| Property | HI | M3 | MC |
|---|---|---|---|
| Density, $g/cm^3$ | 3.03-3.05 | 3.0 | 3.04-3.08 |
| Hardness HK1, GPa, major grains | 20.3 | 21.2 | 19.8-19.9 |
| Hardness HK0.5, GPa, matrix | 14.2 | 12.3 | - |
| Hardness HV1, GPa, major grains | 23.5-23.9 | 23.6 | 22.8-24.4 |
| Hardness HV0.5, GPa, matrix | 14.4-14.5 | - | - |
| Fracture toughness $K_{Ic}$, $MPa.m^{1/2}$, major grains | 2.16-2.38 | 2.51 | 2.4-2.8 |
| Sonic velocity, km/s | 11.6 | 10.3 | 10.5-11.3 |
| Young's modulus, GPa | 390-400 | 305 | 330-375 |
| Flexural strength, MPa | 240 | - | 190 |

Hardness of the matrix for MC ceramics could not be tested due to the structural features of the ceramics

According to Medvedovski (2006) all the studied ceramics have demonstrated a high level of ballistic performance. Armor systems based on alumina based ceramics provide ballistic protection to NIJ Level III or Level IV depending on the type of ceramic and backing material combination. The SiC-based ceramics demonstrate high ballistic protection of NIJ Level III ammunition with multi-hit performance.

Pettersson et al. (2005) explored the use of a material system of Ti-$TiB_2$ in which the hardness of ceramics is combined with the ductility of metals as armor material. The ballistic results indicate a good composition for the outer hardness armor layer. The density of the manufactured material is approximately 4.5 $g/cm^3$ (281 $lb/ft^3$), which is slightly higher than currently used ceramics. For ballistic testing, thin cylindrical discs with a diameter of 38 mm (0.12 ft) and a thickness of 6 mm (0.02 ft) were prepared, ground flat, and glued to thick cylindrical steel backings with a diameter of 40 mm (0.13 ft) and a length of 40 mm (0.13 ft) (Pettersson et al. 2005). Assuming that these dimensions are similar to that of the tested material, then the areal density of the material was approximately 2.7 $g/cm^2$ (5.48 $lb/ft^2$). The test projectile was an armor piercing bullet with a tungsten carbide core. Testing was performed on materials consisting of various weight fraction of titanium. For comparison, Pettersson et al. (2005) manufactured composites by spark plasma sintering (SPS) and hot isostatic pressure. The results of the ballistic testing showed that the SPS material had better protection capability. The following figure gives the ballistic testing results along with hardness and fracture toughness.

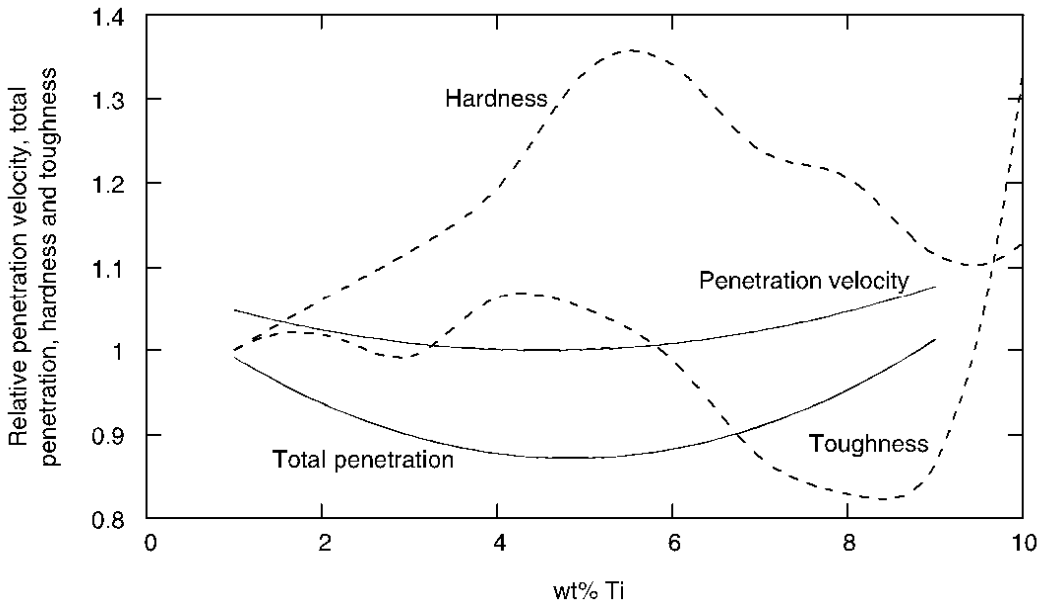


Figure 10: Ballistic testing results plotted along with hardness and fracture toughness (Pettersson et al. 2005)

The penetration depth versus time is evaluated from x-ray images and the penetration velocity is determined by linear regression (Pettersson et al. 2005). A second-degree polynomial is fitted to the average values of penetration velocity and total penetration depth versus titanium content (Pettersson et al. 2005). These polynomials are plotted and fitted according to the least square method together with hardness and fracture toughness in Figure 10. The ballistic results showed that the Ti-$TiB_2$ material is comparable to that of titanium armor.

Risby et al. (2008) presented the potential use of a coconut shell powder-epoxy composite (COEX) bonded with Twaron fabric as a hard armor material. This test panel was found to withstand NIJ Level IIIA equivalent ammunition but perforated when tested with NIJ Level III ammunition. The objective of that study was to investigate the ballistic impact performance of the in-house formulated natural based composite tiles,

which were made from coconut shell powder. Table 8 gives the properties of prepared specimens used in testing.

Table 8: Test specimen classification for testing (Risby et al. 2008)

| Specimen Type | Specimen code | Weight (kg) | Mean thickness (mm) | Length (mm) x Width (mm) | Areal density ($kg/m^2$) |
|---|---|---|---|---|---|
| Twaron panel (5 ply) | TW5 | 0.19 | 3.2 | 300 x 300 | 2.1 |
| Twaron panel (15 ply) | TW15 | 0.51 | 6.1 | 300 x 300 | 5.6 |
| COEX tile format /5ply Twaron | CTW5 | 1.12 | 23.76 | 240 x 180 | 26 |
| COEX tile format/15ply Twaron | CTW15 | 1.33 | 24.99 | 240 x 180 | 30.7 |
| COEX tile format/15ply Twaron | CTW15A | 1.28 | 26.34 | 240 x 180 | 31.2 |
| COEX curvature format/15ply Twaron | CVW15 | 1.34 | 16.65 | 300 x 240* | 18.6 |
| COEX curvature format/15ply Twaron | CVW15A | 1.40 | 17.30 | 300 x 240* | 19.4 |

The COEX material is brittle and behaves similar to ceramic materials. A COEX tile was combined with a 5 ply Twaron plate and tested with NIJ Level IIIA ammunition. This plate had an approximate areal density of 5.5 $lb/ft^2$. The panel back face deflection was 30.8 mm (0.1 ft), which was lower than the 44 mm (0.14 ft) set by the NIJ standard. Additional plates with different configurations were also tested and the test results show a back face deflection less than 44 mm (0.14 ft). When compared with ceramic materials, the COEX and Twaron fabrics are not able to fully absorb and dissipate the impact energy as well as ceramic armor. Risby et al. (2008) also manufactured a curved COEX/Twaron plate configuration. After testing, it is observed that the curved plate shows no ballistic resistance to NIJ Level IIIA ammunition.

Zhang et al. (2004) presented the study of the preparation and characterization of isocyanate crosslinked silica aerogel monoliths. This work explains how these crosslinked networks yield aerogels which are up to three times more dense than native aerogels based on the underlying silica framework, but also up to ten times less

hygroscopic while taking more than 300 times the force to break (Zhang et al. 2004). Zhang et al. (2004) explained that the desirable properties of silica aerogels stem from the significant amount of mesoporosity. Figure 11 shows this mesoporosity where secondary particles consist of smaller primary particles of compact silica (Zhang et al. 2004).

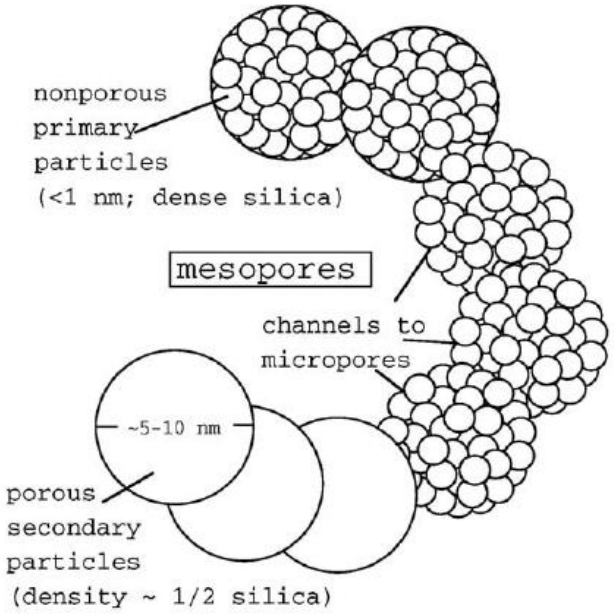


Figure 11: Nanostructure of mesoporous silica (Zhang et al. 2004)

Zhang et al. (2004) explained when a silica aerogel monolith breaks under force, only secondary particles lose contact with one another, while the primary particles remain undisturbed. Therefore, by adding a material conformally to the secondary particles, the bulk structure of the silica aerogel network would be reinforced while the mesoporous space between these particles would be maintained (Zhang et al. 2004). For this study, Zhang et al. (2004) prepared native silica wet gels using two different methods: one step gels via a base-catalyzed route and two-step gels via a modification to the process used by Tillotson and Hrubesh (1992). Crosslinked aerogels were prepared by introducing and

letting an isocyanate react with the mesoporous surfaces of native silica wet gels (Zhang et al. 2004). Chemical characterization of crosslinked aerogel monoliths and all control samples was conducted by infrared and $^{13}$C-NMR spectroscopy (Zhang et al. 2004). Physical characterization of native and crosslinked silica aerogel samples was conducted by thermo gravimetric analysis (TGA), NMR imaging, scanning electron microscopy (SEM), nitrogen-adsorption porosimetry, three-point flexural bending and dielectric testing (Zhang et al. 2004). In this study, isocyanate crosslinked aerogels were characterized macroscopically, microscopically and chemically. For macroscopic characterization, the NMR image of the crosslinked monolith is about five percent darker relative to the native wet gel with a calculated void space of ~80 – 86%; therefore, they consist of mostly empty space despite the increase in density (Zhang et al. 2004). For microscopic characterization, the Brunauer-Emmet-Teller (BET) surface-area analysis and average pore-diameter data show that as density increases the total surface area decreases while the average pore diameter increases (Zhang et al. 2004). Zhang et al. (2004) explored hydrophilicity of native and crosslinked aerogels by monitoring the relative water uptake from a water-vapor-saturated environment at room temperature over a period of three days. The results concluded that native silica aerogels take up 50 – 80% of their weight in water while the most dense crosslinked aerogels take up only 2 – 8% water, indicating that they are up to 10 times less hydrophilic (Zhang et al. 2004). In their study, Zhang et al. (2004) also performed dielectric testing of isocyanate crosslinked silica aerogels. Zhang et al. (2004) explain that an ideal insulator for fast electronics requires a relative dielectric constant close to that of air. Since aerogels consist of >90% space filled with air, their relative dielectric constant should be in the range of one to two

and be ideal materials for such applications (Zhang et al. 2004). Zhang et al. (2004) chose to explore whether or not an increase in density and strength, making the material processing, compromises the dielectric properties. The results of their study conclude that the relative dielectric constant calculated has a value of $2.0 \pm 0.1$, therefore, the dielectric properties are not compromised by crosslinking (Zhang et al. 2004). Finally, Zhang et al. (2004) determined that polymerization of isocyanates template to the surface of a silica network reinforces aerogels by a factor of ~300 with a much smaller increase in density by only a factor of approximately three.

# 3. METHODOLOGY

## 3.1 Simulation Method

ABAQUS Explicit 6.8-3 was used to simulate the armor plate configuration. Figure 12 is the configuration for the armor plate which was simulated using ABAQUS.

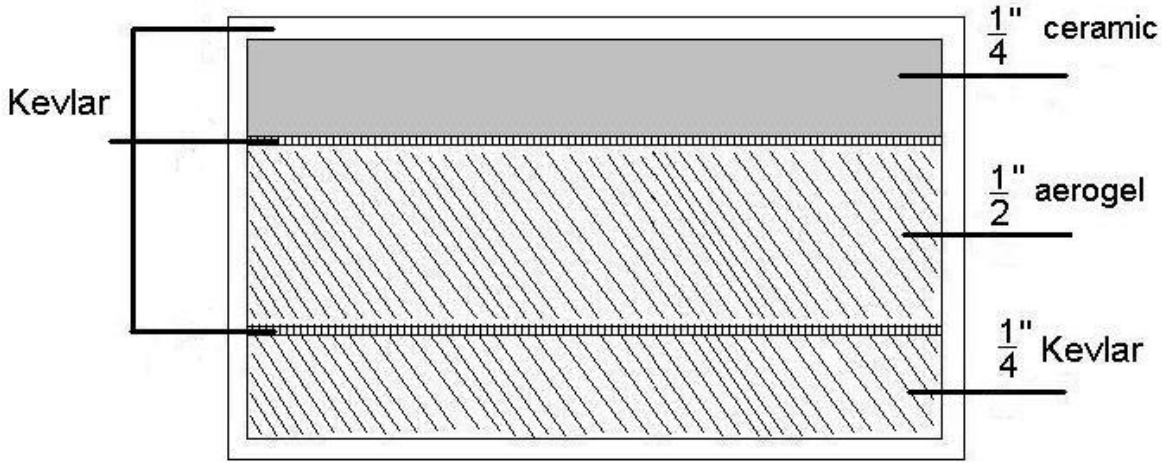


Figure 12: Level III armor plate configuration consisting of ceramic, aerogel, and Kevlar.

Due to symmetry, the armor plate model in ABAQUS was ¼ of the actual armor plate with fixed boundary conditions along the perimeter of the plate. The configuration of the ABAQUS model from the front of the plate to the back is as follows: 0.003 m (0.125 inch) Kevlar wrapping, 0.006 m (0.25 inch) Silicon Carbide ceramic tile, 0.012 m (0.5 inch) Aerogel, 0.006 m (0.25 inch) Kevlar composite plate, 0.003 m (0.125) Kevlar

wrapping. Figure 13 shows the Kevlar sheet before it was wrapped around the armor plate.

Figure 13: Dry woven Kevlar used for wrapping around the armor plate.

The materials used in the armor plate are given in Table 9. Table 9 lists manufacturer information, areal density of material, and model number if applicable.

Table 9: Manufacturer, areal density, and model number of materials used in the manufacturing of the armor plate.

| Material | Dimensions (L × W × H) | Manufacturer | Areal Density | Model |
|---|---|---|---|---|
| Dry woven Kevlar | 0.53 m × 0.15 m × 0.51 mm<br><br>21" × 6" × 0.02" | Hexcel<br>www.hexcel.com<br>Annette Ramsey<br>830-379-1580<br>aramsey@jpscm.com | 3.7 kg/m$^2$<br><br>(0.75 lb/ft$^2$) | 745 |
| Silicon Carbide Ceramic Tile | 0.15 m × 0.15 m × 0.006 m<br><br>6" × 6" × 0.25" | Saint Gobain<br>www.saint-gobain.com<br>Bob Palia<br>716-278-6006<br>scd.sales@saint-gobain.com | 20 kg/m$^2$<br><br>(4.07 lb/ft$^2$) | Hexoloy Sintered |
| Aerogel plate | 0.15 m × 0.15 m × 0.01 m<br><br>6" × 6" × 0.4" | Oklahoma State University | 9.05 kg/m$^2$<br><br>(1.84 lb/ft$^2$) | MP4 – T045 |
| Laminated Kevlar (composite plate) | 0.15 m × 0.15 m × 0.008 m<br><br>6" × 6" × 0.31" | Hexcel<br>www.hexcel.com<br>Annette Ramsey<br>aramsey@jpscm.com | 8.02 kg/m$^2$<br><br>(1.63 lb/ft$^2$) | 745 CS 4735 |

The lead core of a 0.308 Winchester bullet is used in the simulation with a mass of 11.66 grams (0.026 lb) and a velocity of 847 m/s (2778.9 ft/s). Figure 14 shows the lead core of a 7.62 mm (0.025 ft) NATO bullet along with the copper jacket.

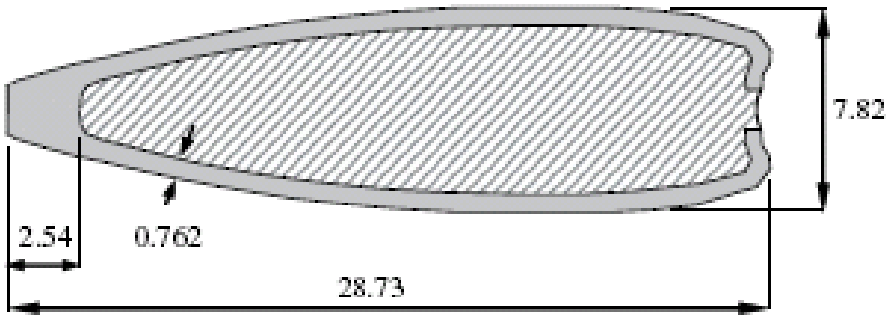


Figure 14: 7.62 mm NATO bullet - lead core along with copper jacket (dimensions are in mm)

The 7.62 mm NATO bullet has the same dimensions and characteristics as the 0.308 Winchester bullet used in testing. The manufactured armor plate was created based on the simulation results from ABAQUS. The configuration of the developed armor plate consists of Silicon Carbide ceramic tile, crosslinked aerogel, ballistic grade Kevlar composite plate, and a ballistic grade one-ply Kevlar sheet for wrapping. All layers were bonded using 3M$^{TM}$ Scotch-Weld$^{TM}$ DP110 Epoxy Adhesive. The Silicon Carbide ceramic tile was ballistic grade and was obtained from Saint Gobain Ceramics. The ceramic tile had dimensions of 0.15 × 0.15 × 0.006 m (6 × 6 × 0.25 inch). The ceramic tile was cleaned with acetone and bonded to a single layer of Kevlar via 3M$^{TM}$ Scotch-Weld$^{TM}$ DP110 Epoxy Adhesive.

## 3.2 Preparation of Polyurea Crosslinked Templated Aerogels

All templated mesoporous materials of this study were made by initially dissolving 4.0 g (0.1 oz) of Pluronic P123 (Sigma Aldrich, St. Louis, MO), used in as received form, in 12 g (0.42 oz) of a 1.0 M aqueous solution of nitric acid (Fisher Scientific, Pittsburgh, PA), diluted with deionized water, under magnetic stirring. The mixture was cooled to 0°C via an ice bath for approximately 5 minutes. Under magnetic stirring, 0.45 g (0.016 oz) of Mesitylene (TMB, Acros Organics, New Jersey), used in as received form, was added to the cooled mixture. Solutions after addition of Pluronic P123 are clear but after addition of TMB look turbid. After stirring for 30 min, 5.15 g (0.18 oz) of Tetramethylorthosilicate (TMOS, Sigma Aldrich, St. Louis, MO), used in as received form, was added under magnetic stirring. After stirring for an additional 10 minutes at 0°C, the resultant homogeneous solutions were poured into polypropylene molds. Molds

were sealed and kept at 60 °C for gelation. The resulting wet gels were aged at 60 °C for about 5 times the gelation time. After aging, the wet gels were removed from the molds directly into ethyl alcohol ($C_2H_5OH$, Pharmco-AAPER, Brookfield, CT), used in as received form. Ethanol (equal to 4× the volume of the gels) was changed two times in 8 h intervals, and subsequently all wet gels went through a Soxhlet extraction for 3 days in acetonitrile ($CH_3CN$, Pharmco-AAPER, Brookfield, CT), used in as received form. After the Soxhlet extraction, wet gels were washed with acetone ($OC(CH_3)_2$), Pharmco-AAPER, Brookfield, CT), used in as received form, four times with a wash duration of 8 hours. The samples were placed in an acetone and hexamethylene diisocyanate oligomer (Desmodur N3200, Bayer MaterialScience, Pittsburgh, PA), used in as received form, solution. The volume of the acetone was 4.5× the volume of the gels. The concentration of N3200 was 11/94 × the volume of acetone. After allowing a 36 hour equilibration time in the corresponding N3200 solution, samples were heated together with the surrounding N3200 solution at 55 °C for three days. After four more acetone washes (~8 h each time, using each time a volume of acetone equal to 4× the volume of the gels) to remove unreacted diisocyanate, gels were washed 4 × with Pentane ($C_5H_{12}$, Pharmco-AAPER, Brookfield, CT), used in as received form. After the $4^{th}$ wash, the gels were removed from Pentane and allowed to air dry for two days. After drying, the crosslinked aerogel plates were machined to dimensions of approximately 6" × 3" × 0.2".

Split Hopkinson Pressure Bar (SHPB) tests were also performed on the crosslinked aerogel used in the armor. The stress strain relationship is shown in Figure 15.

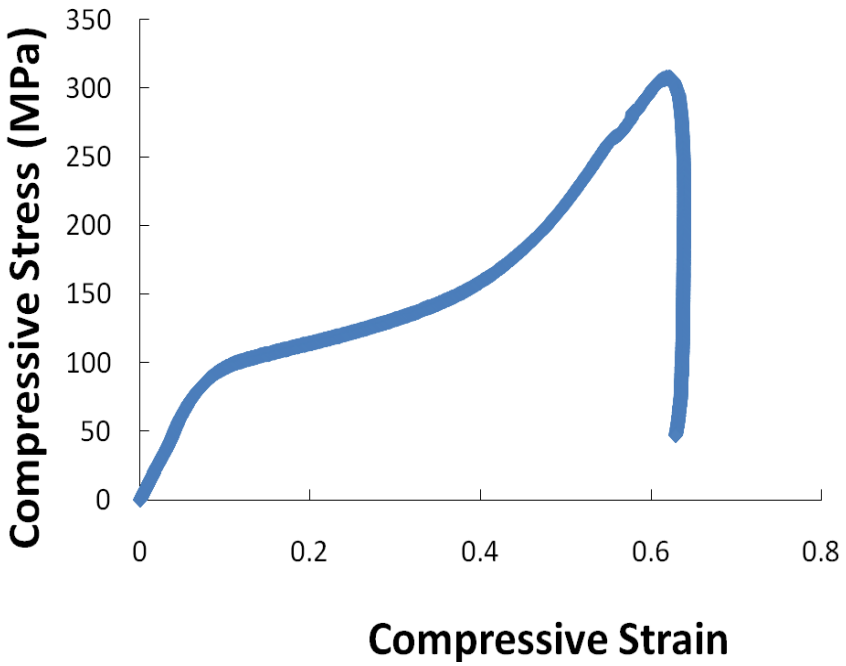


Figure 15: Stress Strain relationship for crosslinked aerogel (X-MP4-T045, density = 0.66 g/cm$^3$) at strain rate 1600/s.

From Figure 15, it is concluded that crosslinked aerogels behave linearly under tension while they fail in brittle mode. The Young's modulus and tensile strength for this material are approximately 1224 MPa and 308 MPa, respectively.

## 3.3 Preparation of Armor Plate 1

The manufactured aerogel plates were attached to each other via 3M™ Scotch-Weld™ DP110 Epoxy Adhesive to form one large aerogel plate with dimensions of 0.15 m × 0.15 m × 0.01 m (6" × 6" × 0.4"). The aerogel plate was then bonded to two layers of ballistic grade Kevlar, one on the top of the aerogel plate and one on the bottom. A ballistic grade composite Kevlar plate was manufactured by bonding layers of laminated Kevlar. The laminated Kevlar as cut into 0.15 m × 0.15 m (6" × 6") squares. The Kevlar layers were stacked and placed under vacuum during a set curing temperature. The ceramic plate,

aerogel plate, Kevlar composite plate, and two Kevlar plies were bonded together via 3M™ Scotch-Weld™ DP110 Epoxy Adhesive. Figure 16 is an image of all components after bonding.

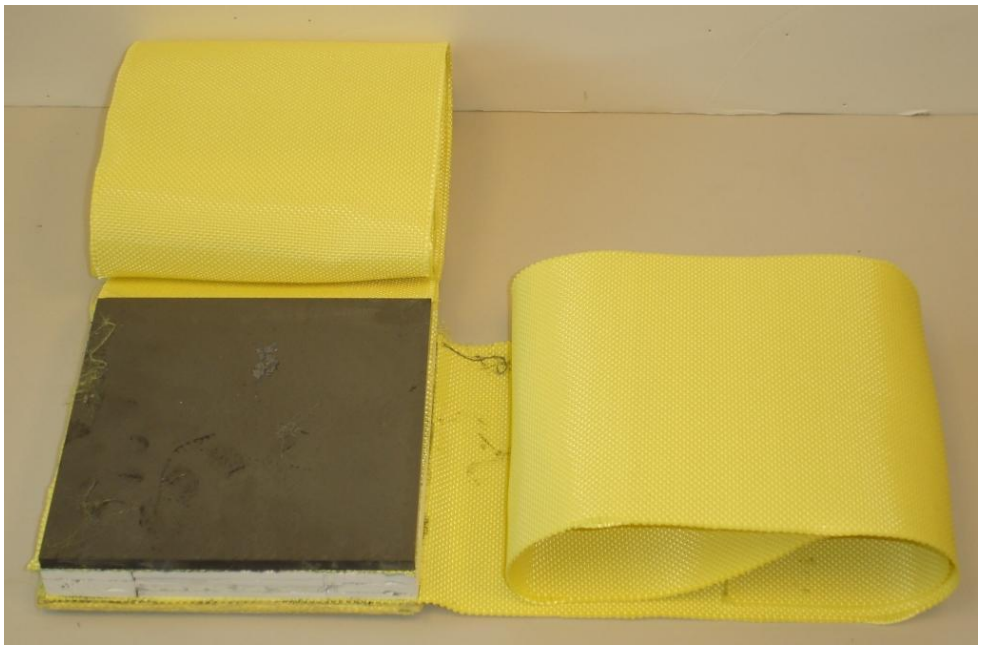

Figure 16: All elements of the armor plate bonded together in the following order: SiC ceramic tile, Kevlar strip, aerogel plate, Kevlar strip, and Kevlar composite plate.

The excessive Kevlar strips were wrapped tightly around the armor plate to form one solid armor plate. Figure 17 shows the final armor plate after assembly.

Figure 17: Final armor plate 1 with dimensions of 0.16 m × 0.16 m × 0.04 m (6.25" × 6.25" × 1.48") and a total areal density of 4.3 g/cm$^2$ (8.2 lb/ft$^2$).

## 3.4 Preparation of Baseline Armor Plate

A baseline armor plate which is known to stop an NIJ Level III bullet was manufactured for comparison. After the baseline plate was tested, the test results could be compared to an aerogel incorporated armor plate. The baseline armor plate consisted of a 0.003 m (0.25 inch) thick SiC ceramic tile, a 0.003 m (0.25 inch) thick Kevlar composite plate, and a Kevlar fabric wrapping similar to that of Armor Plate 1. Figure 18 shows the configuration of the baseline plate.

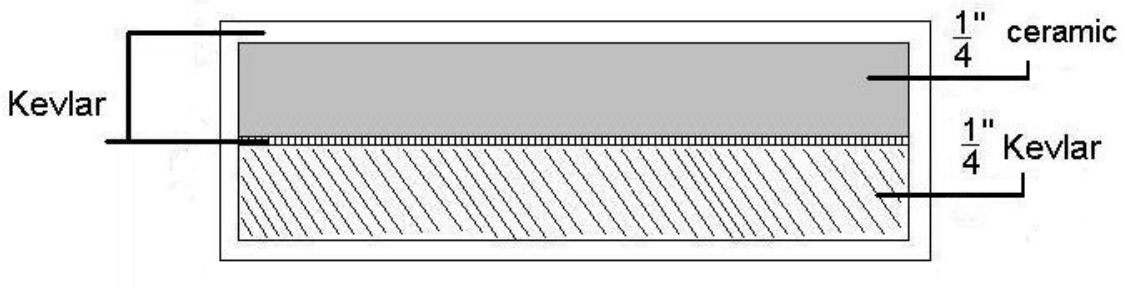


Figure 18: Level III baseline armor plate configuration consisting of ceramic and Kevlar.

The baseline armor plate, after manufacturing, had a volume of 396 $cm^3$ (0.014 $ft^3$), a weight of 685 g (1.51 lbs), and an areal density of 29.79 $kg/m^2$ (6.06 $lb/ft^2$). The final dimensions of the armor plate were 0.16 m × 0.16 m × 0.02 m (6.1" × 6.1" × 0.65").

## 3.5 DSM Dyneema

DSM Dyneema is the inventor and manufacturer of an ultra-strong, lightweight polyethylene fiber known as Dyneema® HB51 (Luykx et al., 2009). It is up to 15 times stronger than high quality steel and up to 40% stronger than aramid fibers (Luykx et al., 2009). Dyneema® floats on water and is extremely durable and resistant to moisture, UV light and chemicals (Luykx et al., 2009). For our testing, the Unidirectional (UD) Dyneema® Hard Ballistic #51 (HB51) product is incorporated into the armor plate to provide a lighter weight armor with similar ballistic performance when compared to an armor plate containing SiC ceramic tile. This material provides an ideal combination of enhanced ballistic performance and lightweight comfort (Luykx et al., 2009). In a Dyneema® UD product all the fibers are laid parallel, in the same plane, rather than being woven together (DSM Dyneema, 2009). Dyneema® UD is made of several layers of Dyneema® fibers, with the direction of fibers in each layer at 90° to the direction of

the fibers in the adjacent layers (DSM Dyneema, 2009). The unidirectional configuration of the fibers in Dyneema® UD allows the energy transferred from the impact of a bullet or other threat to be distributed along the fibers much faster and more efficiently than in conventional woven fabrics (DSM Dyneema, 2009). This is because the absorption power of the yarn in woven fabrics is lost at the crossover points, as these points reflect rather than absorb the shockwaves of the impact (DSM Dyneema, 2009). In Dyneema® UD, much more of the material is engaged in stopping the bullet, making it more effective against ballistics (DSM Dyneema, 2009).

## 3.6 Preparation of Armor Plate 2

Since Dyneema® provides the same ballistic performance as SiC ceramic tile, with less weight; it is incorporated into the armor plate instead of the ceramic tile. Current research suggests that Dyneema® alone with an areal density of 16 kg/m$^2$ (3.25 lb/ft$^2$) can stop NIJ Level III ammunition. Since this amount of HB51 can independently stop an NIJ Level III bullet, the HB51 is combined with an aerogel backing to decrease the back face deflection of the body armor. Figure 19 shows the configuration of the body armor plate consisting of Dyneema® HB51, aerogel, and Kevlar.

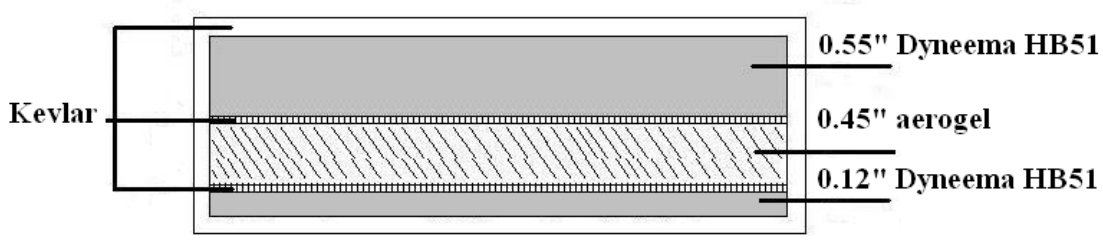


Figure 19: Level III Armor Plate 2 configuration consisting of Dyneema, aerogel, and Kevlar with dimensions of 0.32m × 0.31m × 0.04m (12.6" × 12.25" × 1.47") and an areal density of 33.43 kg/m$^2$ (6.8 lb/ft$^2$).

All layers of Armor Plate 2 are bonded together using epoxy and wrapped with Kevlar fabric in the same manner as all other armor plates.

## 3.7 Preparation of Armor Plate 3

The performance of Dyneema® is not confirmed, so an additional plate incorporating a different thickness of Dyneema® HB51 was manufactured. Armor Plate 3 incorporates a thicker Dyneema® plate which should easily stop an NIJ Level III bullet. For this armor plate, aerogel is included so that the back face deflection is minimized. Figure 20 shows the configuration of the body armor plate consisting of Dyneema® HB51, aerogel, and Kevlar.

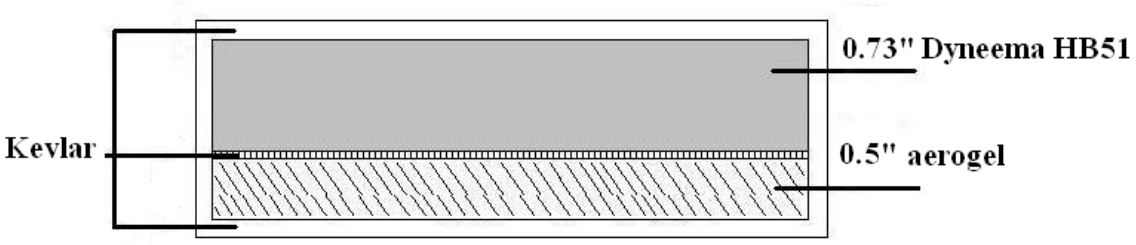


Figure 20: Level III Armor Plate 3 configuration consisting of Dyneema, aerogel, and Kevlar with dimensions of 0.31m × 0.32m × 0.04m (12.2" × 12.4" × 1.4") and an areal density of 33.72 kg/m$^2$ (6.86 lb/ft$^2$).

All layers of Armor Plate 3 are bonded together using epoxy and wrapped with Kevlar fabric in the same manner as all other armor plates.

# 4. FINDINGS

## 4.1 FEM Simulation

The FEM simulation, in ABAQUS, models ¼ of the armor plate with fixed boundary conditions along the perimeter of the plate. Figure 21 is the FEM model used in ABAQUS.

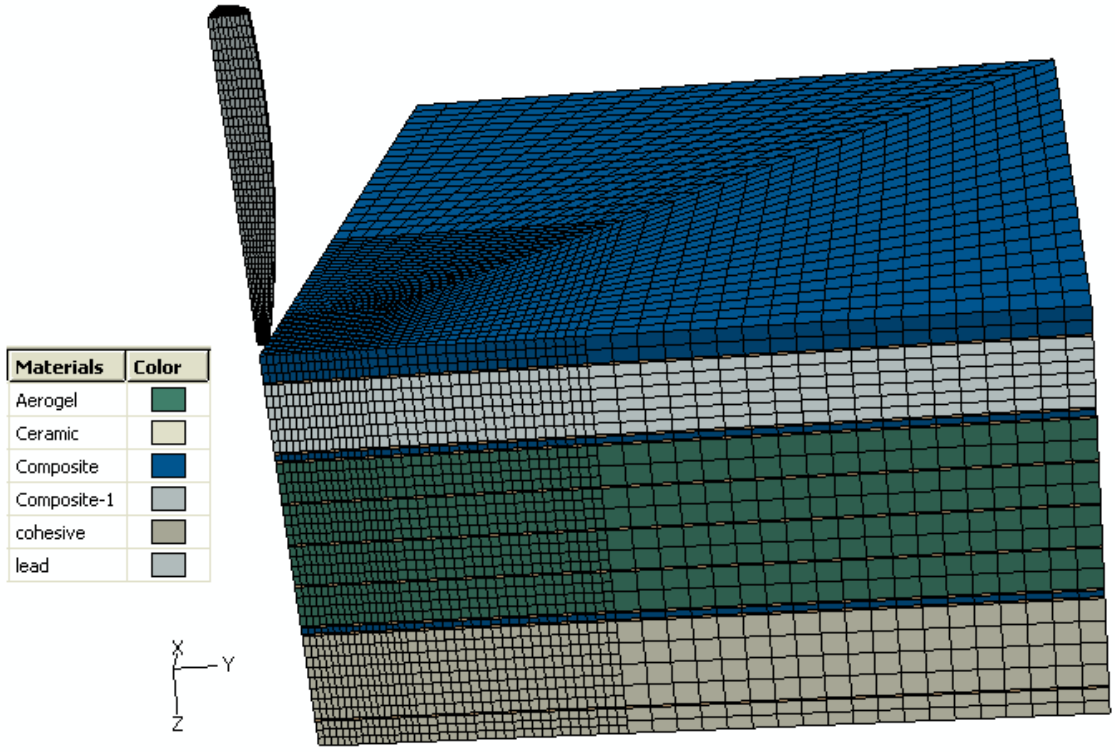


Figure 21: FEM model of armor plate

The material properties are given in Table 10.

Table 10: Material Properties used in the FEM model of the armor plate

| Material | Mass Density (mm) | Young's Modulus (GPa) | Poisson's Ratio |
|---|---|---|---|
| Aerogel | 670 | 1.73 | 0.2 |
| Ceramic | 3100 | 410 | 0.14 |
| Kevlar | 1300 | 75 | 0.3 |
| Composite Plate | 1300 | 75 | 0.3 |
| Epoxy Resin | 1100 | 1 | 0.35 |
| Lead | 9738 | 30 | 0.3 |

The FEM simulation used the Dynamic, Explicit option with a time step of 0.00025 seconds. The bullet velocity used in the simulation was 838 m/s (2750 ft/s). Since the simulation is of complex contact, mesh part along with erode element was used to simulate the armor plate. In addition, it is known that higher stresses will occur at the sight of bullet impact, so a finer mesh was used in this area to better determine the stresses which would be seen during impact. The stress distribution in the armor plate during impact is shown in Figure 22.

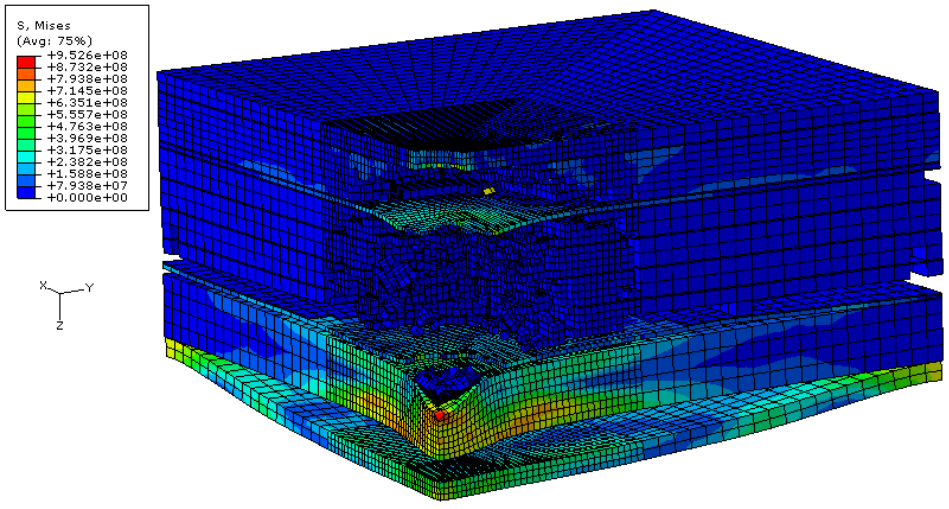


Figure 22: Stress distribution of armor plate in FEM simulation.

The FEM simulation results conclude that the armor plate is able to stop the bullet from penetrating the armor plate. Figure 23, below, is the last frame of the FEM simulation.

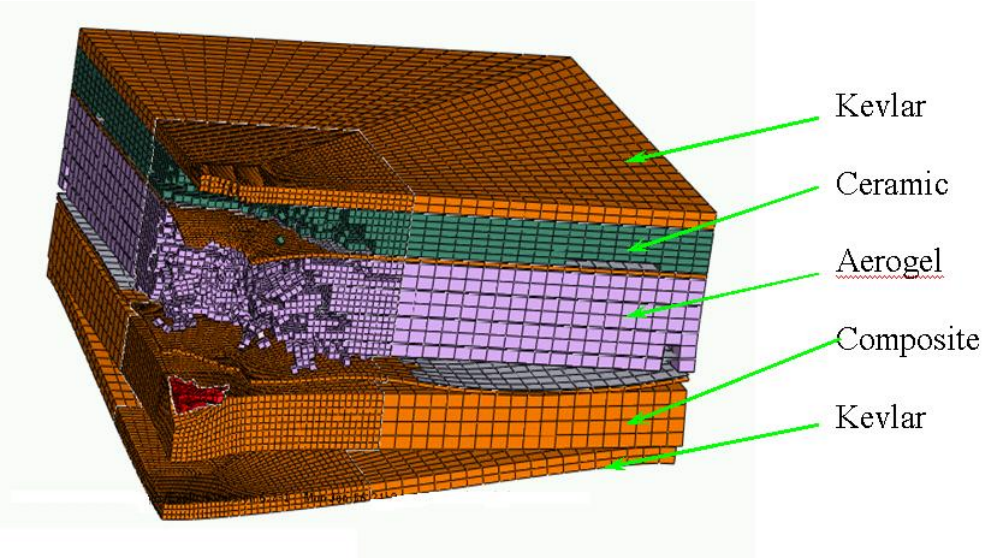


Figure 23: Last frame of the armor plate FEM simulation. The armor plate layers are shown with orange representing Kevlar and the Kevlar composite plate, green represents the ceramic plate, purple represents the aerogel plate, the red represents the bullet, and a slight gray layer is shown which represents an adhesive layer.

According to the simulation model shown schematically in Figure 23, the Silicon Carbide tile is backed by aerogel and Kevlar composite. The armor plate was impacted by a .308 Winchester bullet and the back face deflection was measured. The maximum back face deflection measured from the FEM simulation is approximately 12 mm (0.47 inch).

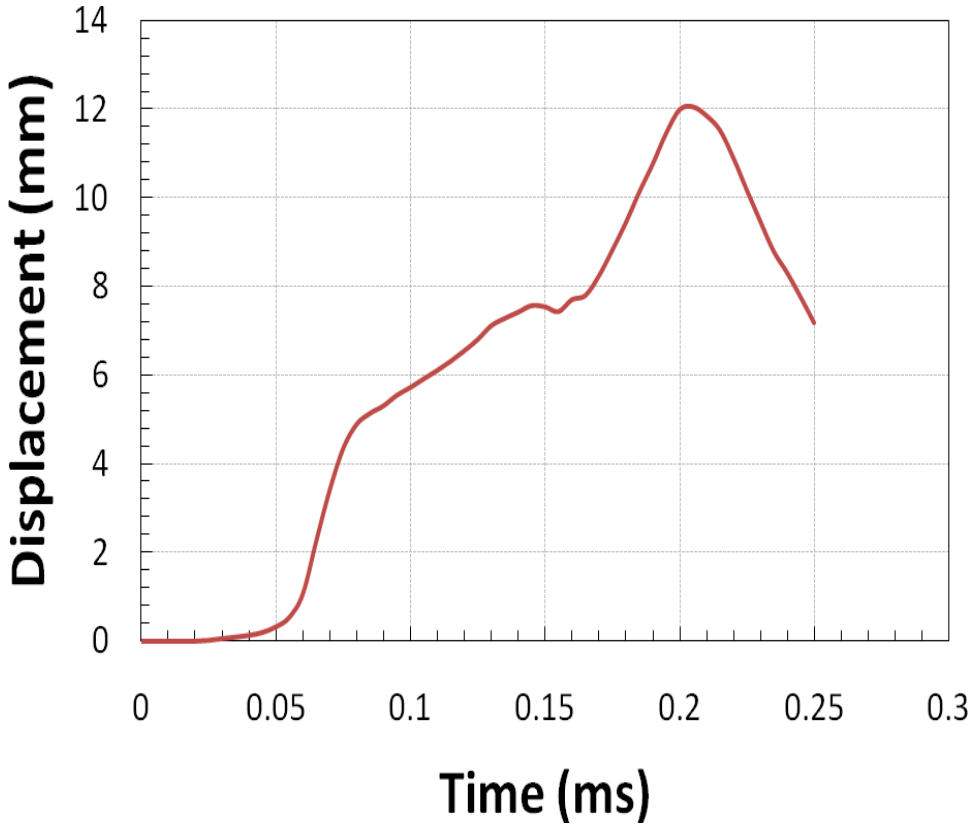


Figure 24: Deformation output from FEM simulation

The displacement of the armor plate as a function of time is shown in Figure 24. The back face deflection occurs at the maximum deformation as shown in the figure. This deformation correlates to the measurement of the back face deflection after the testing of the armor plate was complete. The deflection of the armor plate was measured using digital calipers. The measured back face deflection was 12.7 mm ± 1.3 mm (0.5 inch ± .05 inches). The maximum deflection as shown from the simulation method is 12 mm (0.47 inch). Therefore, the difference between actual deflection and simulated deflection is less than 1 mm (0.04 inch).

## 4.2 Testing Procedures

The NIJ Standard-0101.04 was followed in order to test all manufactured armor plates. The NIJ Standard-0101.04 (2001) states that all armor models submitted to NIJ for compliance testing will undergo a series of ballistic impact tests using the ammunition specified in Table 11 and Table 12.

Table 11: Test Variables as stated in the NIJ Standard-0101.04 (NIJ 2001).

| Test Variables | | | | |
|---|---|---|---|---|
| **Armor Type** | **Test Round** | **Test Bullet** | **Bullet Weight** | **Reference Velocity (± 30 ft/s)** |
| IIIA | 1 | 9 mm FMJ RN | 8.2 g 124 gr. | 436 m/s (1430 ft/s) |
| | 2 | 44 Mag SJHP | 15.6 g 240 gr. | 436 m/s (1430 ft/s) |
| III | 1 | 7.62 mm NATO FMJ | 9.6 g 148 gr. | 847 m/s (2780 ft/s) |

Table 12: Performance Requirements as stated in the NIJ Standard-0101.04 (NIJ 2001).

| Performance Requirements | | | | | | | |
|---|---|---|---|---|---|---|---|
| **Armor Type** | **Hits Per Armor Part at 0° Angle of Incidence** | **BFS Depth Maximum** | **Hits Per Armor Part at 30° Angle of Incidence** | **Shots Per Panel** | **Shots Per Sample** | **Shots Per Threat** | **Total Shots Req'd** |
| IIIA | 4 | 44 mm (1.73 in) | 2 | 6 | 12 | 24 | 48 |
| | 4 | 44 mm (1.73 in) | 2 | 6 | 12 | 24 | |
| III | 6 | 44 mm (1.73 in) | 0 | 6 | 12 | 12 | 12 |

These impact tests measure two back face deflections and demonstrate the armor's pass/fail penetration capability (NIJ 2001). This test series requires the use of a

plastically deforming clay backing material held in direct contact with the back surface of the armor panel (NIJ 2001). This configuration is used to capture and measure the back face deflection depression produced in the backing material during nonperforating threat round impacts (NIJ 2001). A backing material fixture was manufactured in accordance with the NIJ standard. The standard states that the inside dimensions of the backing material fixture shall be 610 mm x 610 mm x 140 mm ± 2 mm (24.0 in x 24.0 in x 5.5 in ± 0.06 in) deep (NIJ 2001). The tolerance on all dimensions will be ± 2 mm (0.06 in) (NIJ 2001). The back of the fixture shall be removable and constructed of 19.1 mm (0.75 in) thick wood or plywood (NIJ 2001). The sides of the box fixture shall be constructed of rigid wood or metal, preferably with a metal front edge to reliably guide the preparation of the flat front surface of the backing material (NIJ 2001). The backing material shall be worked into the fixture with as few voids as possible (NIJ 2001). The backing material surface shall be cut or otherwise manipulated to result in a smooth, flat front surface even with the front edges of the box fixture (NIJ 2001). The NIJ Standard states that Roma Plastilina No.1 oil-based modeling clay is acceptable for the backing material application (NIJ 2001). For this study, the Roma Plastilina No.1 oil-based modeling clay was purchased through Sculpture House® (Sculpture House, Inc., 405 Skillman Road, PO Box 69, Skillman, NJ 08558. Phone: 609-466-2986. Email: customercare@sculpturehouse.com. Website: www.sculpturehouse.com). During testing, the bullet velocity must be recorded. The standard states that a chronograph used to record the measurement will, as a minimum, be capable of recording to 0.3 m/s (1.0 ft/s) (NIJ 2001). For this study a PACT Model 1 XP Chronograph with Improved Sky screen Mounting Bracket was purchased and used in all testing of the armor plates

(www.pact.com). The standard also specifies the configuration in which the chronograph must be set up. The first chronograph start trigger screen will be placed at either 2 m (6.5 ft) or 12.2 m (40 ft) from the muzzle of the test barrel as shown in Figure 25.

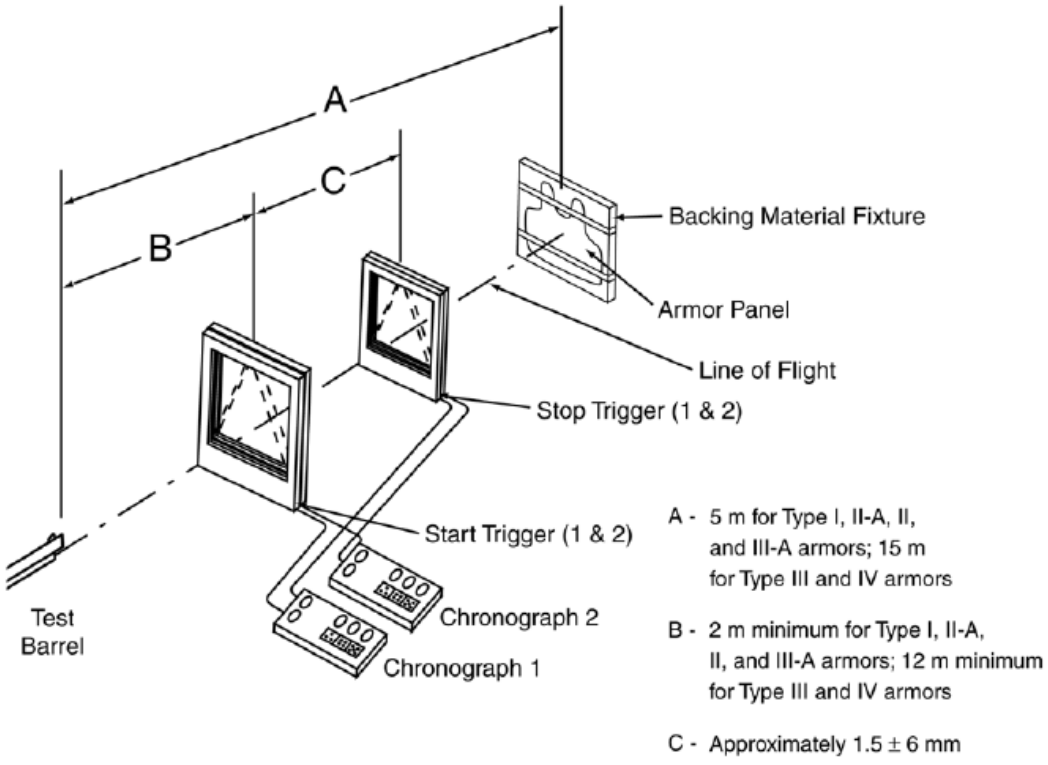


Figure 25: Test range configuration as stated by the NIJ Standard (NIJ 2001).

The screens will be arranged so that they define vertical planes perpendicular to the line of flight of the bullet (NIJ 2001). The screens will be securely mounted to maintain their required position and spacing (measurement accuracy of ± 1 mm (± 0.04 in)) (NIJ 2001). The testing range was set up according to the standard so that the test equipment is placed as shown in Figure 25. In addition, the test barrel was mounted on an appropriate fixture with the barrel horizontal (NIJ 2001). Dimensions A and B were measured from the barrel muzzle (NIJ 2001). The backing material fixture was be rigidly held by a metal

test stand. The standard states that the metal test stand should permit the entire armor and backing material assembly to be shifted vertically and horizontally such that the entire assembly can be targeted by the test barrel (NIJ 2001). However, in our testing where the backing material fixture was used, the metal test stand was not able to shift in any direction. Due to the stationary metal stand, all bullet velocity calibrations were performed at a different location than where the armor plates were tested. Due to this move in setup, the velocity measurements may not be completely accurate. When the testing setup is moved, all angles of incidence with respect to the armor plate and the test barrel are changed. This change in angle could greatly change the bullet velocity calculation.

## 4.3 Armor Plate 1

The ceramic tile used in armor plate 1 had dimensions of 0.15 m × 0.15 m × 0.006 m (6" × 6" × 0.25" inch). The size of the ceramic tile was chosen in such a way to provide multi-hit protection, which is a requirement of the NIJ Standard-0101.04. The ballistic efficiency of the ceramic tile is expected to provide realistic behavior as if it were to be used in actual applications. The armor panel was prepared by bonding each layer together using 3M™ Scotch-Weld™ DP110 Epoxy Adhesive. The armor plate was then wrapped four times with a piece of dry woven Kevlar. Experiments were performed in the Stillwater Police Department firing range where the .308 Winchester was fired using a police sniper rifle. The lead core is covered with a copper sheath and has a diameter of 7.9 mm (0.31 inch); length of the core being approximately 27.6 mm (1.09 inch) and it weighs 11.66 g (0.03 lb).

Figure 26: 0.308 Winchester bullet: the copper covered lead core of the bullet has a diameter of 7.9 mm (0.31 inch), a length of 27.6 mm (1.09 inch), and weighs 11.66 g (0.03 lb). The bullet has a muzzle velocity of approximately 798.6 m/s (2620 ft/s).

Figure 26 is a photograph of the .308 Winchester bullet and core. The mass of the shot (core + copper sheath) is about 11.66 g (0.03 lb). The bullet was fired at an approximate velocity of 906.8 m/s (2975 ft/s). The velocity was measured to an accuracy of ± 43.3 m/s (142 ft/s). After the experiment is performed, it is noted that the bullet did not penetrate the armor plate. Figure 27, below, are images taken of Armor Plate 1 after testing.

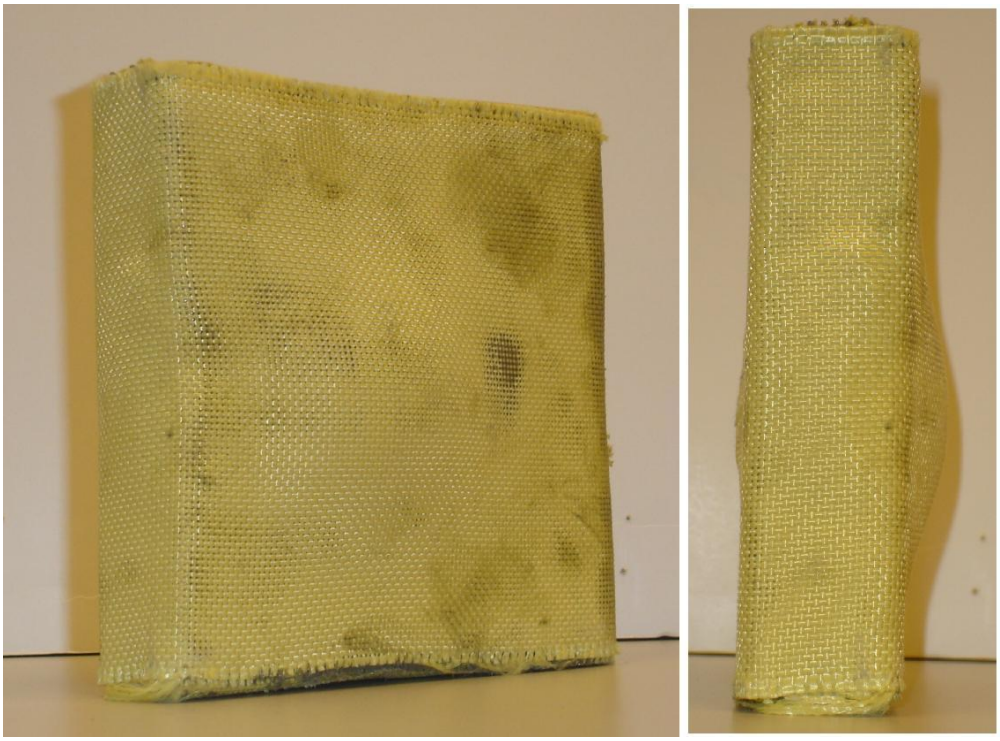

Figure 27: Tested Armor Plate 1 with back face deflection

The back face deflection of the armor plate is clearly seen. The deflection of the armor plate was measured using digital calipers. The measured deflection is 12.7 mm ± 1.3 mm (0.5 inch ± .05 inches). The areal density of current body armor is 17.2 kg/$m^2$ – 22 kg/$m^2$ (3.5 – 4.5 lb/ $ft^2$). The body armor developed in this study has an areal density of 40.3 kg/$m^2$ (8.2 lb/$ft^2$).

After testing the armor plate, the plate underwent a Computerized Tomography Scan (CT scan). The CT scan recorded approximately 320 images total with the images split between three axes. The CT scan allows the deformation patterns of the ceramic and aerogel to be seen. In addition, the bullet and bullet fragments can be seen in the images but not with pure clarity. Wilkins (1978) and Shockey (1990) have provided notable description of the ballistic failure processes in ceramic-faced armors. According to Wilkins (1978), the projectile tip is destroyed first. According to Madhu (2005), a fracture conoid initiates at the interface between the projectile and the target. The cones developed from impact spread the load of the projectile onto a wide area allowing the energy to be absorbed by ductile backing material. As shown in Figure 28, the very bright areas are thought to be the deformed bullet and bullet fragmentation.

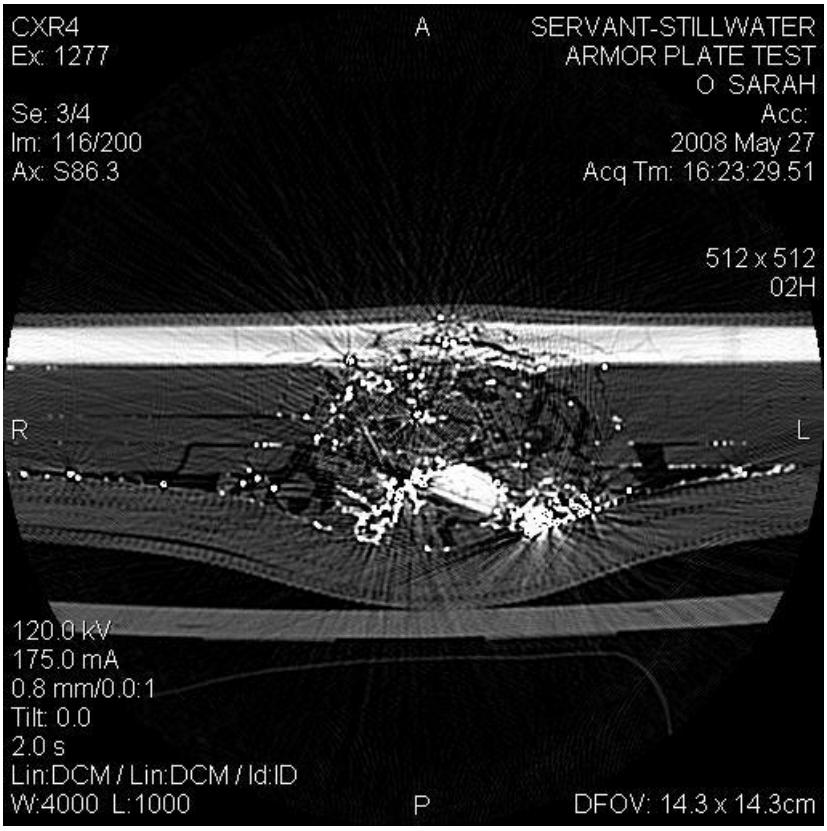


Figure 28: CT scan image of deformed armor plate. A Hitachi CXR4, 4 slice CT, was used for the imaging of the armor plate. The images were taken at 120 kV and 175 mA. The images were taken at a resolution of 512 × 512.

The largest, brightest spot in the center of the armor plate is considered to be the deformed bullet. The spot is conical in shape and would represent a bullet which is deformed after impact. In addition, it seems that the bullet rotated during its travel into the armor plate since the back of the bullet (flat side) is directly opposite from the point of entry into the armor plate (top surface).

Since the CT images were taken on three different axes, the fracture patterns of the ceramic tile are easily seen. A series of radial cracks form in the ceramic tiles as a result of bullet penetration. These radial cracks can be seen easily in Figure 29.

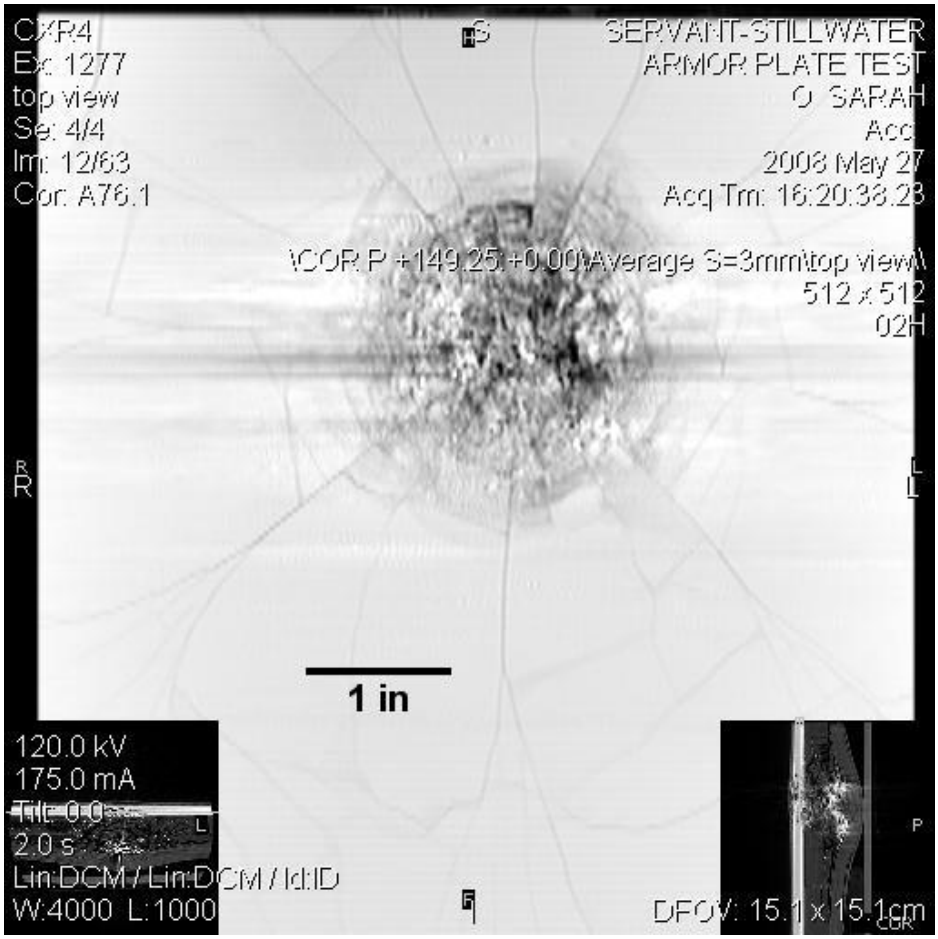


Figure 29: CT scan image of deformed ceramic plate

## 4.4 Baseline Armor Plate

The ceramic tile used in the baseline armor plate had dimensions of 0.15 m × 0.15 m × 0.006 m (6" × 6" × 0.25" inch). The size of the ceramic tile was chosen in such a way to provide multi-hit protection, which is a requirement of the NIJ Standard-0101.04. The ballistic efficiency of the ceramic tile is expected to provide realistic behavior as if it were to be used in actual applications. The armor panel was prepared by bonding each layer together using 3M™ Scotch-Weld™ DP110 Epoxy Adhesive. The baseline armor plate was then wrapped four times with a piece of dry woven Kevlar. Experiments were

performed in the Tulsa Shooting Academy firing range where the M80 NATO Ball was fired using a rifle provided by the Academy. The M80 NATO Ball has specifications similar to that of the 0.308 Winchester bullet. After the experiment is performed, it is noted that the bullet did not penetrate the armor plate. Figure 30 is the baseline armor plate after testing.

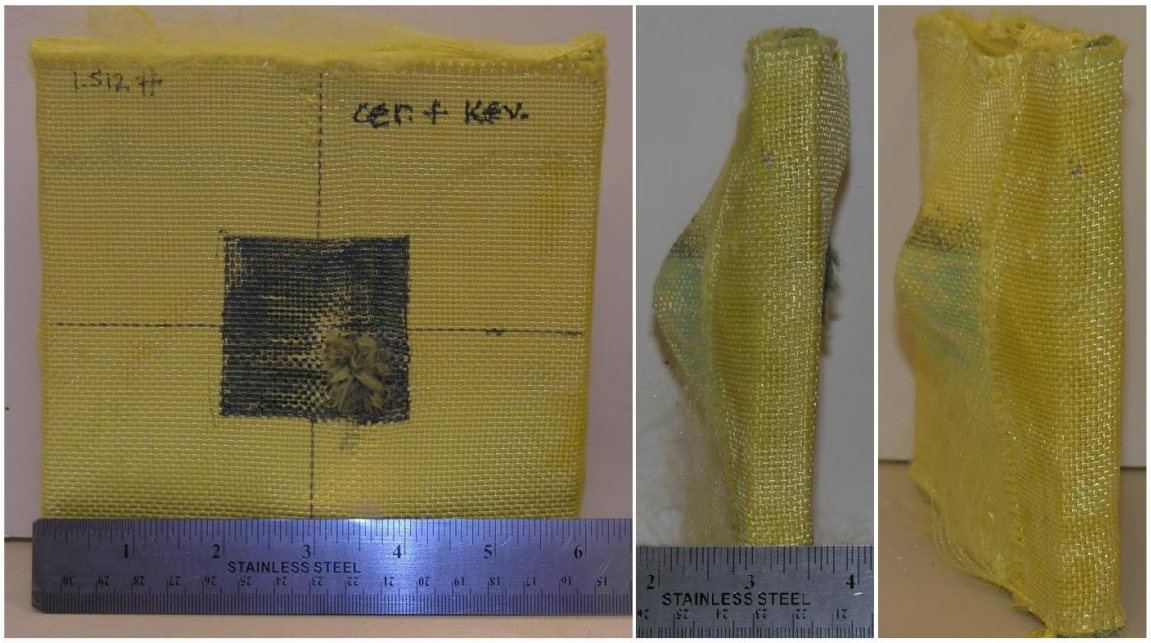


Figure 30: Tested baseline armor plate with back face deflection

The deflection of the armor plate was measured using digital calipers. The measured deflection is 30.5 mm ± 2.54 mm (1.2 in ± .1 in). The baseline armor plate had an areal density of 29.8 kg/m$^2$ (6.06 lb/ft$^2$).

After testing the armor plate, the plate underwent a Computerized Tomography Scan (CT scan). The CT scan recorded approximately 227 images total with the images split between three axes. The CT scan allows the deformation patterns of the ceramic to be

seen. In addition, the bullet and bullet fragments can be seen in the images with slight clarity. As shown in Figure 31, the very bright areas with light diffraction are thought to be the deformed bullet and bullet fragmentation.

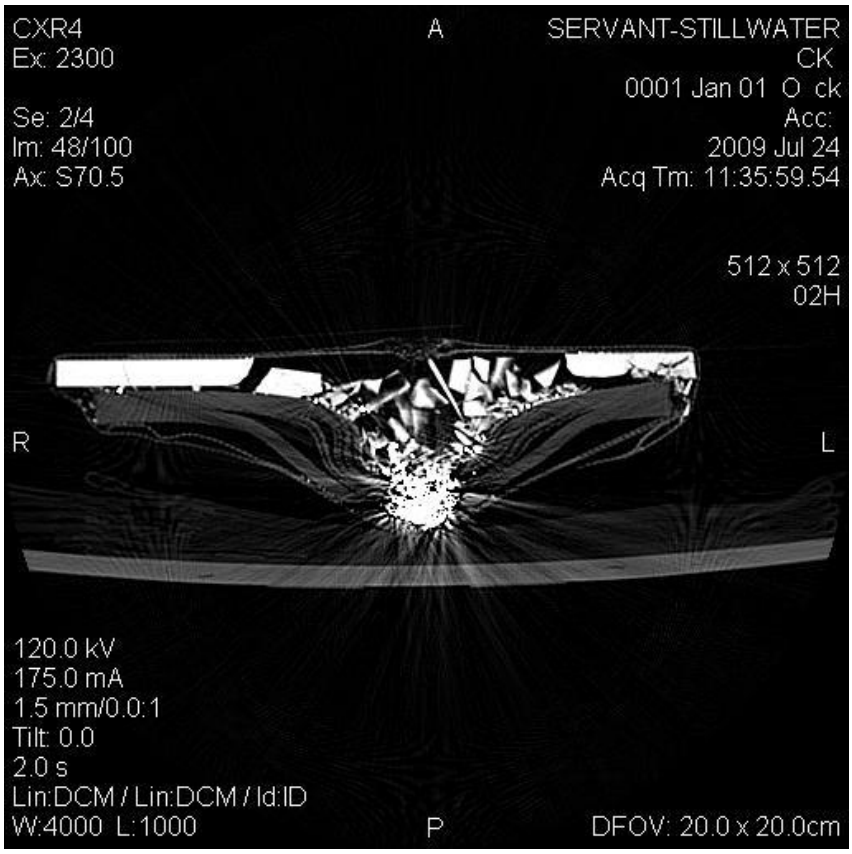


Figure 31: Baseline Armor Plate

The bright white sections are the ceramic tile. The largest, brightest spot in the center of the armor plate is considered to be the deformed bullet. The spot is round in shape, but not perfectly round which would represent a bullet that was deformed at impact. From the CT scan, most of the ceramic tile is deformed and de-lamination can be seen in the layers of the Kevlar composite plate. In addition, the bullet almost penetrates the Kevlar composite plate. The back face deflection of the armor plate was also measured and

estimated from the CT scan. The measured back face deflection from the CT scan is approximately 28 mm (1.1 in). This measurement is very close to that of the deflection measured using calipers.

## 4.5 Armor Plate 2

Armor Plate 2 was tested at the US Shooting Academy in Tulsa, OK. The armor plate was tested with an M80 NATO Ball. The bullet was fired at an approximate velocity of 740 m/s (2428 ft/s). After the experiment is performed, it is noted that the bullet did not penetrate the armor plate. Figure 32, below, are images taken of Armor Plate 2 after testing.

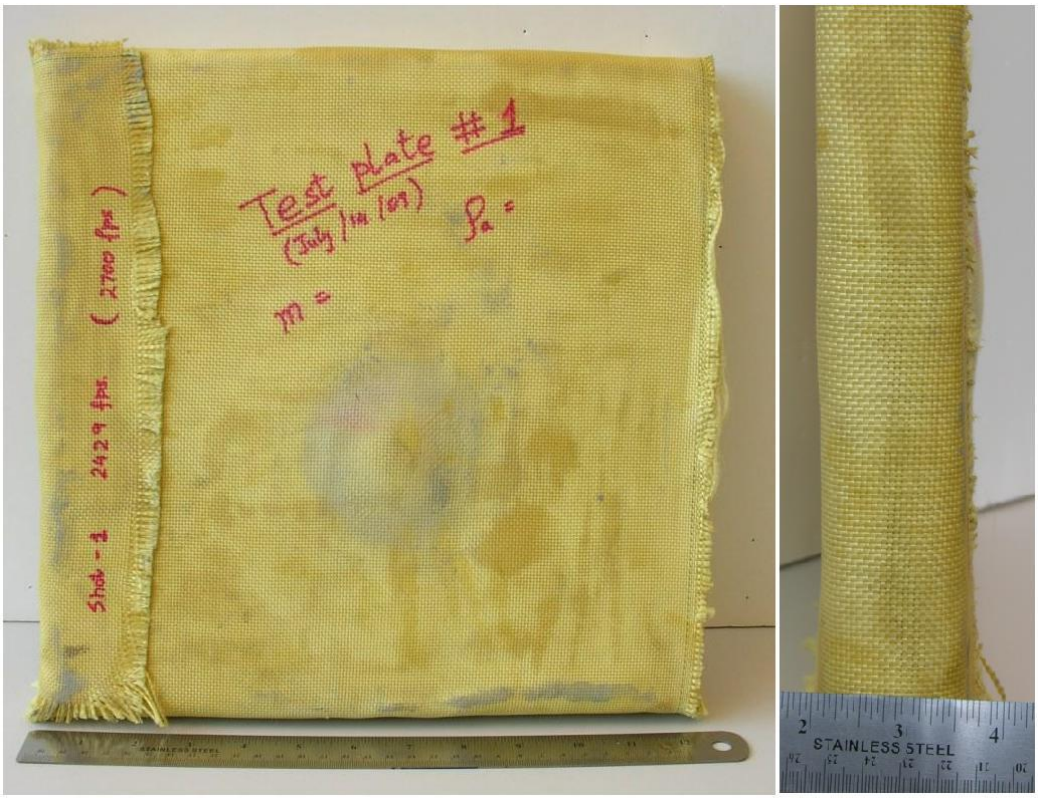


Figure 32: Tested Armor Plate 2 with back face deflection.

The back face deflection of the armor plate is not as clearly seen as the previous armor plate. The measured deflection is approximately 4.06 mm (0.16 in). This body armor plate has an areal density of 33.4 kg/m$^2$ (6.8 lb/ft$^2$). As stated in the NIJ Standard-0101.04, all armor plates should be tested on a clay backing. The clay backing simulates trauma to the body. In this case, the back face deflection in the clay backing was 18 mm (0.71 in).

After testing the armor plate, the plate underwent a Computerized Tomography Scan (CT scan). The CT scan recorded approximately 227 images total with the images split between three axes. The CT scan allows the deformation patterns of the Dyneema® and aerogel to be seen. In addition, the bullet and bullet fragments can be seen in the images with fair clarity. As shown in Figure 33, the very bright, shiny area is the bullet.

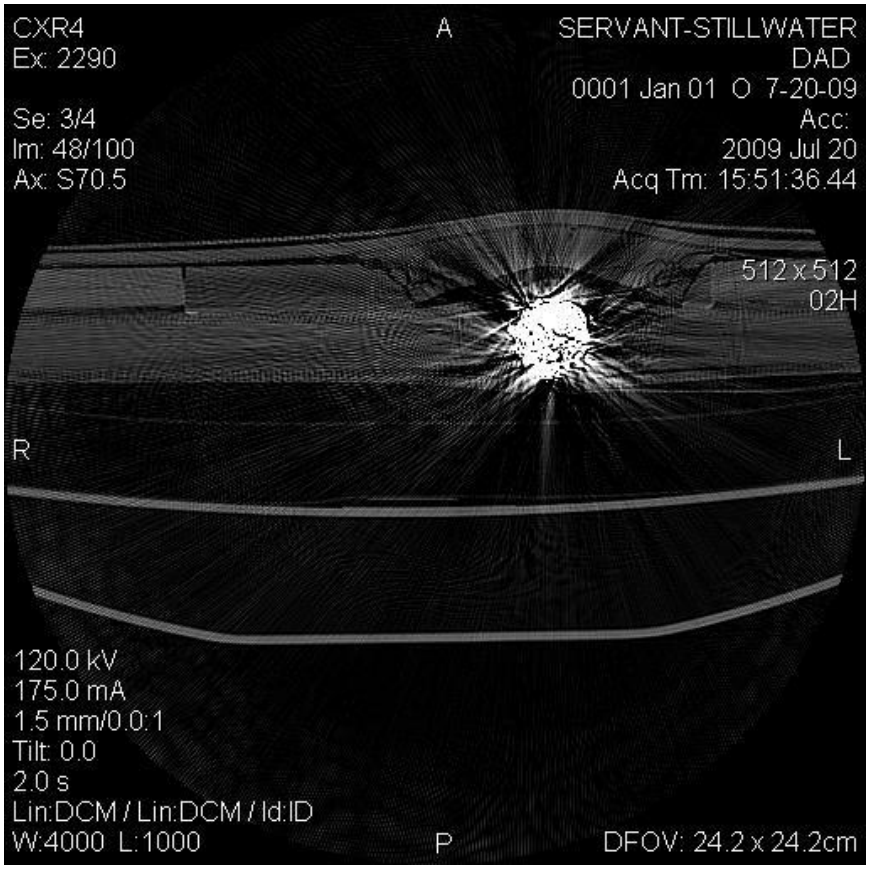


Figure 33: CT scan image of deformed Armor Plate 2.

The largest, brightest spot in the center of the armor plate is considered to be the bullet. As seen in the CT image, the bullet appears to be rounded. There are no other bright spots around the bullet which means no fragmentation occurred. As observed by the CT image, the bullet underwent no deformation. An estimate in the back face deflection can be measured from the CT scan. The back face deflection was measured from the CT scan to be 10.16 mm (0.4 in). In addition, it is noted that approximately 4.06 mm (0.16 in) of the Dyneema® is un-penetrated.

## 4.6 Armor Plate 3

Armor Plate 3 was tested at the US Shooting Academy in Tulsa, OK. The armor plate was tested with an M80 NATO Ball. The bullet was fired at an approximate velocity of 788 m/s (2585 ft/s). After the experiment is performed, it is noted that the bullet did not penetrate the armor plate. Figure 34, below, are images taken of Armor Plate 3 after testing.

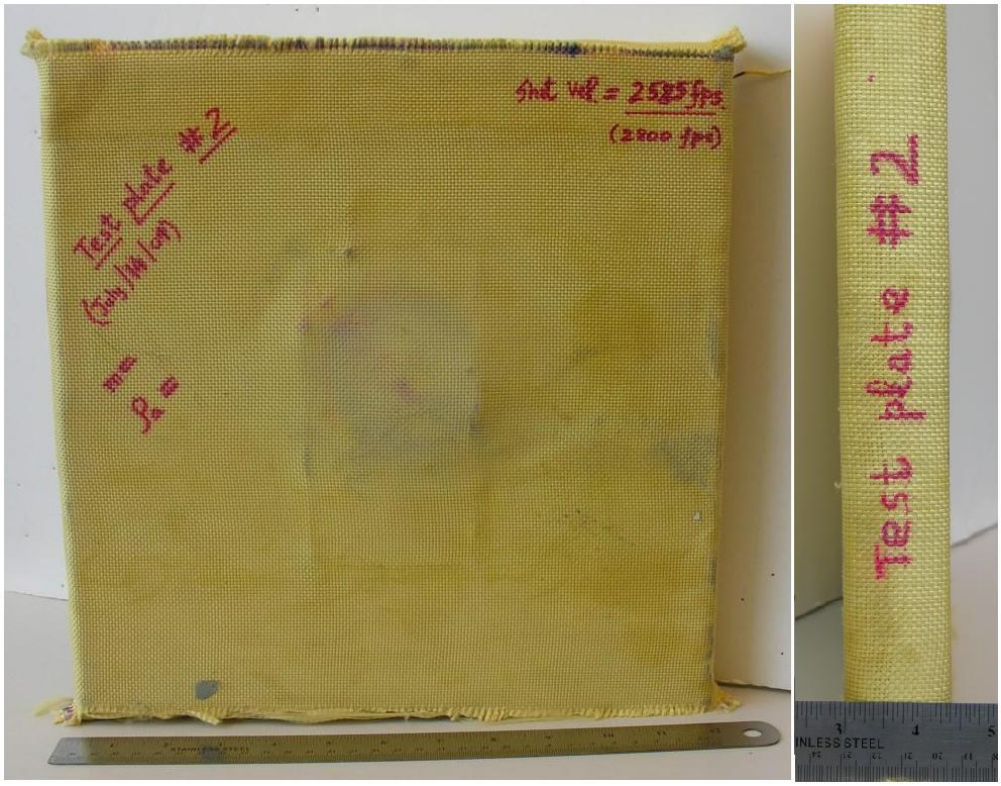


Figure 34: Tested Armor Plate 3 with back face deflection.

The back face deflection of the armor plate is barely seen. The measured deflection is approximately 3.3 mm (0.13 in). This body armor plate has an areal density of 33.7 kg/m$^2$ (6.86 lb/ft$^2$). As stated in the NIJ Standard-0101.04, all armor plates should be

tested on a clay backing. The clay backing simulates trauma to the body. In this case, the back face deflection in the clay backing was 22 mm (0.87 in).

After testing the armor plate, the plate underwent a Computerized Tomography Scan (CT scan). The CT scan recorded approximately 202 images total with the images split between three axes. The CT scan allows the deformation patterns of the Dyneema® and aerogel to be seen. In addition, the bullet can be seen in the images with fair clarity. As shown in Figure 35, the very bright, shiny area is the bullet.

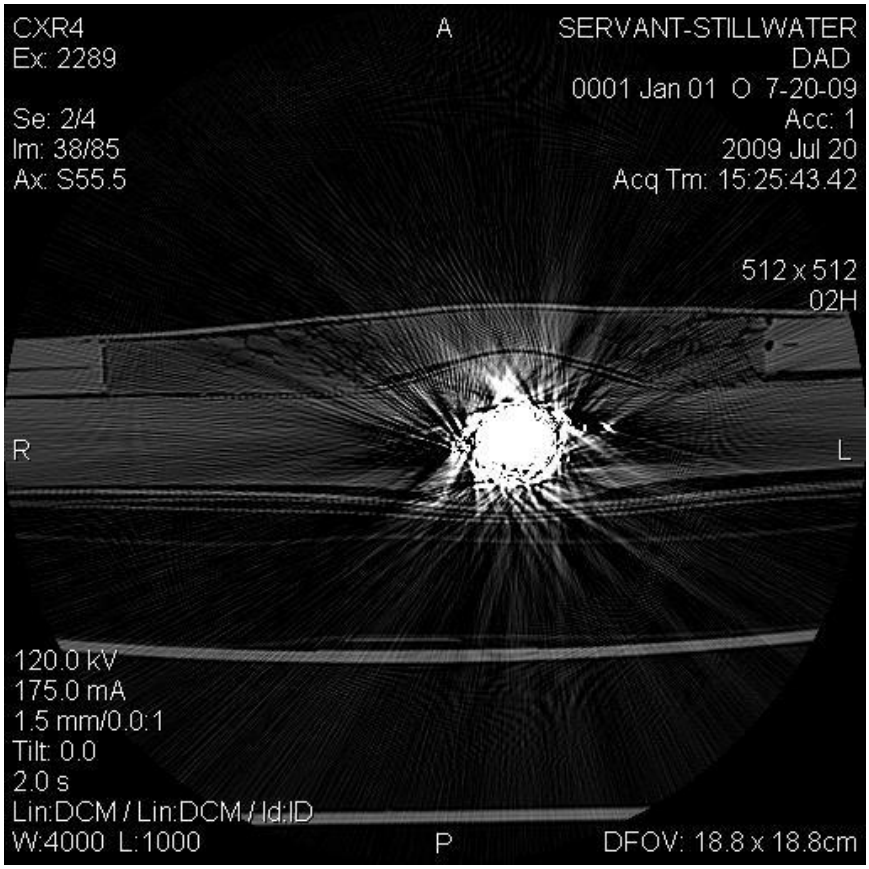


Figure 35: CT scan image of deformed Armor Plate 3

The largest, brightest spot in the center of the armor plate is considered to be the bullet. As seen in the CT image, the bullet appears to be rounded. There are no other bright spots around the bullet which means no fragmentation occurred. As observed by the CT image, the bullet underwent no deformation. The back face deflection was measured from the CT scan to be 6.1 mm (0.24 in). In addition, it is noted that approximately 10.16 mm (0.4 in) of the Dyneema® is un-penetrated.

## 4.7 Baseline Dyneema® Plate

The baseline Dyneema® armor plate was tested at the US Shooting Academy in Tulsa, OK. The armor plate was tested with an M80 NATO Ball. The bullet was fired at an approximate velocity of 780 m/s (2560 ft/s). After the experiment is performed, it is noted that the bullet did not penetrate the armor plate. Figure 36, below, is an image taken of the baseline Dyneema® armor plate after testing.

Figure 36: Tested baseline Dyneema® armor plate with back face deflection of armor plate as well as back face deflection in the clay backing material.

The back face deflection of the armor plate is clearly seen. The measured deflection is approximately 13.46 mm (0.53 in). The baseline Dyneema® armor plate has an areal density of 16.71 kg/m$^2$ (3.4 lb/ft$^2$). As stated in the NIJ Standard-0101.04, all armor plates should be tested on a clay backing. The clay backing simulates trauma to the body. In this case, the back face deflection in the clay backing was 32 mm (1.26 in).

After testing the armor plate, the plate underwent a Computerized Tomography Scan (CT scan). The CT scan recorded approximately 193 images total with the images split between three axes. The CT scan allows the deformation Dyneema® to be seen as well as any de-lamination that occurs in between the layers of Dyneema®. In addition, the bullet can be seen in the images with fair clarity. As shown in Figure 35, the very bright, shiny area with light diffraction is the bullet along with any bullet fragmentation.

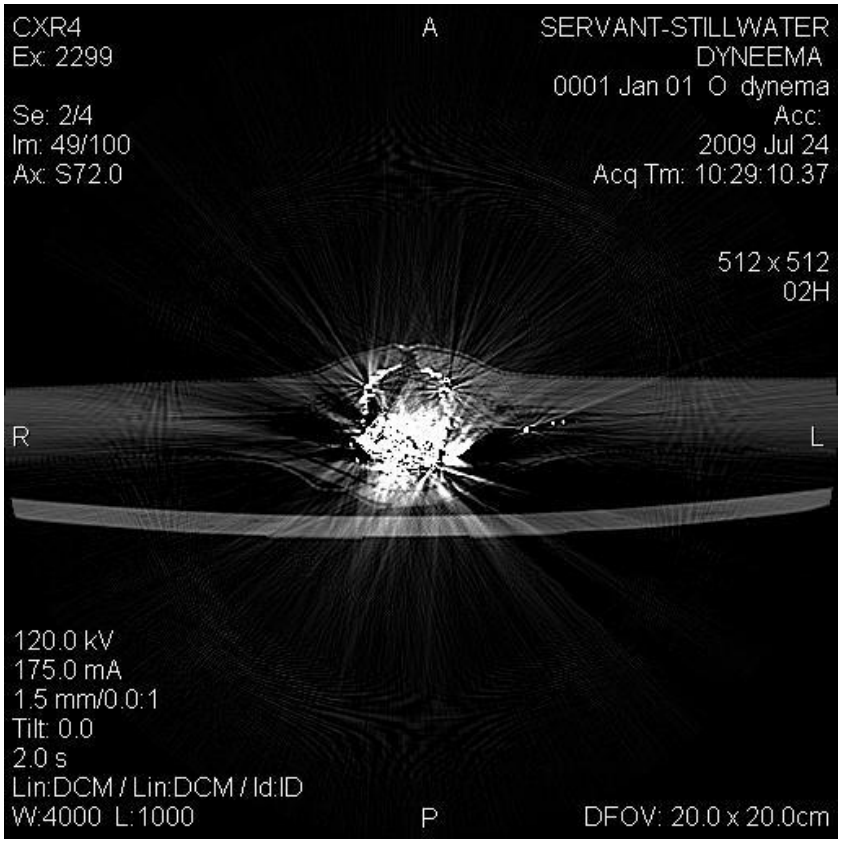


Figure 37: CT scan image of deformed Dyneema® baseline Armor Plate

The largest, brightest spot in the center of the armor plate is considered to be the bullet. As seen in the CT image, the bullet appears to be somewhat rounded. Additionally, there are bright spots around the bullet which indicates fragmentation has occurred. As observed by the CT image, the bullet underwent slight deformation. The back face deflection measured from the CT scan is approximately 12 mm (0.47 in). In addition, it is noted that approximately 7.11 mm (0.28 in) of the Dyneema® is un-penetrated.

# 5. CONCLUSION

Improvements in military body armor are essential for the safety, security, and comfort of military personnel. Many military fatalities and injuries occur from body armor failure as well as ammunition fragmentation. Most ammunition fragmentation hit parts of the body which are not covered with armor. A solution to this is a very lightweight body armor that could cover more areas of the body without weighing more than current armor. The goal of this study was to develop a lightweight body armor which is able to stop military ranked ammunition. An armor plate was developed using ballistic grade ceramic tile, aerogel, and ballistic grade Kevlar. Although the weight of the armor plate is larger than the military body armor currently used, the back face deflection is quite small. The FEM simulation results gave a back-face deflection of 12 mm (0.47 in) and the actual back face deflection of the tested armor plate was 12.7 mm (0.5 in). The armor plate yielded a back face deflection 5.8% greater than the simulation result. The CT scan images show a large deformation in the bullet which is a result of its penetration into the armor plate. A baseline armor plate was manufactured without aerogel to compare the effect that the aerogel had on energy absorption. The baseline armor plate was assumed to stop the bullet. The baseline plate testing stopped the bullet and resulted in a back face deflection of 28mm (1.1 in). The back face deflection of the baseline armor plate is 120% greater than the armor plate containing aerogel. From this test, it is concluded that the aerogel contributes a significant amount of energy absorption and contributes to a reduction in

the back face deflection. From this, it was observed that the ceramic tile and aerogel absorbed most of the energy from the bullet impact. After comparing all tested armor plates to current body armor standards, all armor plates exhibit a back face deflection smaller than what is required by the NIJ Standard-0101.04. The back face deflection limit as set by the NIJ Standard-0101.04 is 44 mm (1.73 in). All tested armor plates result in a 36.4% - 72.7% reduction in back face deflection as compared to the standard deflection of 44 mm (1.73 in).

The outcome of the armor plates containing the Dyneema® HB51 is as expected according to recent research. Recent research has suggested that the Dyneema® HB51 with an areal density of approximately 16 kg/m$^2$ (3.25 lb/ft$^2$) can independently stop a bullet. From the CT images, the bullet was contained within the Dyneema® HB51. It is also observed that the aerogel backing did not undergo as much compression as expected. When comparing the Dyneema® HB51 baseline plate to the armor plate containing both Dyneema® HB51 and aerogel, it is observed that the back face deflection of the armor plate containing aerogel is much smaller than the Dyneema® HB51 baseline armor plate. The tested Dyneema® HB51 baseline plate had a back face deflection of 13.46 mm (0.53 in). The armor plate containing aerogel and Dyneema® HB51 had a back face deflection of 4.06 mm (0.16 in). The comparison of both plates results in a 70% reduction in back face deflection by the plate containing aerogel. In both plates containing Dyneema® HB51, the CT images show that the bullet did not completely penetrate the Dyneema® plate. This would suggest that the thickness of the Dyneema® HB51 plate could be reduced and that the aerogel does not absorb as much energy as anticipated. From the CT

images, the aerogel exhibits little to no compression by the bullet impact. In order for aerogel to contribute to energy absorption, it should be compressed by the bullet impact by at least 50 percent. Therefore, the armor plates containing Dyneema® HB51 are not optimal designs.

# 6. FUTURE WORK

Since the armor plates containing Dyneema® HB51 can stop NIJ Standard Level III ammunition and have a desirable areal density, the armor plates should be optimized to additionally reduce weight and back face deflection. At this point in the study, the mechanical properties of Dyneema® HB51 are unknown. The mechanical properties of Dyneema® HB51 must be categorized in order to properly optimize an armor plate containing this material. Mechanical properties of Dyneema® HB51 can be found by dynamic testing. This would be the first step in optimization of the Dyneema® HB51 material. After mechanical properties of Dyneema® HB51 have been obtained, FEM simulations should be made in order to obtain preliminary testing results before an armor plate is manufactured. In addition, the previous armor plates containing Dyneema® HB51 could be put into an FEM simulation to compare simulation results to results obtained through our testing. Once the FEM simulations are accurately created, the armor plate design containing Dyneema® HB51 could be optimized. By reducing the thickness of the Dyneema® HB51 plate, the use of aerogel for energy absorption could be maximized. From the results of current testing, it is assumed that a reduction in Dyneema® HB51 would allow more of the aerogel to be compressed and contribute to energy absorption as well as a reduction in back face deflection. Once the optimal thickness of Dyneema® HB51 is determined, the thickness and placement of aerogel can then be optimized through the use of an FEM simulation. Once a maximum thickness of

the Dyneema® HB51/aerogel combination is determined, a reduction in the thickness of the materials could be considered in order to decrease the total thickness of the armor plate. After an optimal armor plate to defeat an NIJ Standard Level III has been established, work can begin to design an armor plate which protects against NIJ Standard Level IV ammunition.

## 7. REFERENCES


1. Capadona, Lynn A., M. B. Meador, A. Alunni, E. F. Fabrizio, P. Vassilaras, and N. Leventis. Flexible, low-density polymer crosslinked silica aerogels. Polymer. 2006. 47: 5754 - 5761.

2. DSM Dyneema. "Dyneema® UD." DSM - Dyneema. 23 July 2009 <http://www.dsm.com/en_US/html/hpf/dyneema_ud.htm>.

3. Hazell PJ, M.R. Edwards, H. Longstaff, and J. Erskine. Penetration of a glass-faced transparent elastomeric resin by a lead-antimony-cored bullet. International Journal of Impact Engineering. 2009. 36: 147 - 153.

4. Karamis, M. Baki, A. Alper Cerit, and F. Nair. Mutual Action Between MMCS Structure and Projectile After Ballistic Impact. Journal of Composite Materials. 2008. 42(23): 2483 - 2498.

5. Katti, Atul, N. Shimpi, S. Roy, H. Lu, E. Fabrizio, A. Dass, L. Capadona, and N. Leventis. Chemical, Physical, and Mechanical Characterization of Isocyanate Cross-linked Amine-Modified Silica Aerogels. Chem. Mater. 2006. 18: 285 - 296.

6. Kaufmann, Christian, D. Cronin, M. Worswick, G. Pageau, and A. Beth. Influence of Material Properties on the Ballistic Performance of Ceramics for Personal Body Armor. Shock and Vibration. 2003. 10: 51 - 58.

7. Leventis, Nicholas, S. Mulik, X. Wang, A. Dass, V. Patil, C. Sotiriou-Leventis, H. Lu, G. Churu, and A. Capecelatro. Conformal Polymer Nano-Encapsulation of Ordered Mesoporous Silica Monoliths for Improved Mechanical Properties. Journal of Non-Crystalline Solids. 2008. 354: 632 - 644.
8. Leventis, Nicholas, C. Sotiriou-Leventis, G. Zhang, and A. M. M. Rawashdeh. Nanoengineering strong silica aerogels. Nano Letters. 2002. 2(9): 957 - 960.
9. Leventis, Nicholas. Three-dimensional core-shell superstructures: Mechanically strong aerogels. Accounts of Chemical Research. 2007. 40(9): 874 - 884.
10. Luo, Huiyang, H. Lu, and N. Leventis. The compressive behavior of isocyanate-crosslinked silica aerogel at high strain rates. Mech Time-Depend Mater. 2006. 10: 83 - 111.
11. Luykx, Anouk and J. van Zundert. "DSM Dyneema Introduces Dyneema® HB51 For Best-In-Class Behindstrike-Face Inserts For US Market". DSM Dyneema Press Office. October 9, 2007. Web. July 23, 2009. <http://www.dsm.com/en_US/downloads/hpf/DYNPR109E1007_HB51_AUSA.pdf>
12. Madhu, Vemuri, K. Ramanjaneyulu, T. Balakrisna Bhat, and N.K. Gupta. An Experimental Study of Penetration Resistance of Ceramic Armour Subjected to Projectile Impact. International Journal of Impact Engineering. 2005. 32: 337 - 350.
13. Meador, Mary Ann B., E.F. Fabrizio, F. Ilhan, A. Dass, G. Zhang, P. Vassilaras, J.C. Johnston, and N. Leventis. Cross-linking Amine-Modified Silica Aerogels with Epoxies: Mechanically Strong Lightweight Porous Materials. Chem. Mater. 2005. 17: 1085 - 1098.

14. Medvedovski, Eugene. Advanced Ceramics for Personnel Armor: Current Status and Future. Ceramic Transactions. 2006. 178: 3 - 17.

15. National Institute of Justice. NIJ Standard–0101.04, Ballistic Resistance of Personal Body Armor. 2001.

16. Pettersson, Annika, P. Magnusson, P. Lundberg, and M. Nygren. Titanium-titanium Diboride Composites as Part of a Gradient Armour Material. International Journal of Impact Engineering. 2005. 32: 387 – 399.

17. Risby, M.S., S.V. Wong, A.M.S. Hamouda, A.R. Khairul, and M. Elsadig. Ballistic Performance of Coconut Shell Powder/Twaron Fabric against Non-armour Piercing Projectiles. Defence Science Journal. 2008. 58(2): 248 - 263.

18. Shockey DE, A.H. Marchand, S.R. Skaggs, G.E. Cort, M.W. Burkett, and R. Parker. Failure Phenomenology of Confined Ceramic Targets and Impacting Rods. International Journal of Impact Engineering. 1990. 9(3): 263 - 275.

19. Tillotson, T.M. and L.W. Hrubesh. Transparent ultralow-density silica aerogels prepared by a two-step sol-gel process. Journal of Non-Crystalline Solids. 1992. 145: 44 - 50.

20. Wilkins ML. Mechanics of Penetration and Perforation. International Journal of Engineering Science. 1978. 16: 793 - 807.

21. Zhang, Guohui, A. Dass, A. M. Rawashdeh, J. Thomas, J. A. Counsil, C. Sotiriou-Leventis, E. F. Fabrizio, F. Ilhan, P. Vassilaras, D. A. Scheiman, L. McCorkle, A. Palczer, J. C. Johnston, M. Meador, and N. Leventis. Isocyanate-crosslinked silica aerogel monoliths: preparation and characterization. Journal of Non-Crystalline Solids. 2004. 350: 152 - 164.

VITA

Sarah Elizabeth Staggs

Candidate for the Degree of

Master of Science

Thesis: PENETRATION RESISTANCE OF POLYMER CROSSLINKED AEROGEL ARMOR SUBJECTED TO PROJECTILE IMPACT

Major Field: Mechanical Engineering

Biographical:

Personal Data: Born in Joplin, MO on December 15, 1978, the daughter of James Staggs and Janet Hennigan

Education: Graduated from Sapulpa High School, Sapulpa, OK in May 1997; Graduated from Tulsa Community College in May 2004 with an Associate of Science degree in Mechanical Engineering; Graduated from Oklahoma State University in May 2007 with a Bachelor of Science degree in Aerospace Engineering; Completed the requirements for the Master of Science degree with a major in Mechanical Engineering at Oklahoma State University in July 2009.

Experience: Employed by Oklahoma State University, Stillwater, Department of Mechanical and Aerospace Engineering as a graduate research assistant – 2007 to present.

Professional Memberships: American Society of Mechanical Engineers, American Institute of Aeronautics and Astronautics.

Name: Sarah Elizabeth Staggs Date of Degree: December, 2009

Institution: Oklahoma State University Location: Stillwater, Oklahoma

Title of Study: PENETRATION RESISTANCE OF POLYMER CROSSLINKED AEROGEL ARMOR SUBJECTED TO PROJECTILE IMPACT

Pages in Study: 69 Candidate for the Degree of Master of Science

Major Field: Mechanical Engineering

Scope and Method of Study:

The goal of this study is to develop a body armor prototype which is lightweight, strong, and improves on the back face deflection of current armor. By incorporating ballistic grade ceramic tile, aerogel, and ballistic grade Kevlar a body armor plate was developed which stopped an NIJ Level III bullet with a minimal back face deflection. The armor plate developed has a larger areal density than the current body armor, but the back face deflection is an improvement. Prior to testing, a computer simulation, completed in ABAQUS, was created to understand what results might be expected after testing the armor plate. A new ballistic fiber, Dyneema®, was also introduced into the configuration of the armor plate. The purpose of this fiber was to replace the ceramic tile with the goal of reducing the weight of the body armor further. Since Dyneema® is currently known to stop an NIJ Level III bullet; it was incorporated into an armor plate along with crosslinked aerogels in order to reduce back face deflection.

Findings and Conclusions:

The results given by ABAQUS gave a back-face deflection of 12 mm (0.47 in) and the actual back face deflection of the tested armor plate was 12.7 mm (0.5 in). The armor plate yielded a back face deflection 5.8% greater than the simulation result. After testing all armor plates, they underwent a CT scan, where images in three axes are saved in order to determine the deformation of the ceramic tile, crosslinked aerogel, Kevlar, and Dyneema® plates. In addition, the CT scans allow the deformation of the bullets to be seen. The CT scans also allow the deformation of the aerogel plates to be analyzed in order to optimize energy absorption for future armor plates incorporating crosslinked aerogels. The back face deflection for all tested armor plates could be measured from the CT scans as well as measured manually. All tested armor plates result in a 36.4% - 72.7% reduction in back face deflection as compared to the standard deflection of 44 mm (1.73 in).

ADVISER'S APPROVAL: Hongbing Lu